

RESEARCH ARTICLE | FEBRUARY 25 2025

Hydroelastic performance of an ultra-large containership in irregular and freak waves

Wenjie Zhang (张文杰) ; Yuan Zhuang (庄园) ; Decheng Wan (万德成) ; Jianhua Wang (王建华)  



Physics of Fluids 37, 027190 (2025)

<https://doi.org/10.1063/5.0254680>



Articles You May Be Interested In

KoopmanLab: Machine learning for solving complex physics equations

APL Mach. Learn. (September 2023)

Experimental realization of a quantum classification: Bell state measurement via machine learning

APL Mach. Learn. (September 2023)



Physics of Fluids

Special Topics Open
for Submissions

[Learn More](#)



Hydroelastic performance of an ultra-large containership in irregular and freak waves

Cite as: Phys. Fluids **37**, 027190 (2025); doi: [10.1063/5.0254680](https://doi.org/10.1063/5.0254680)

Submitted: 24 December 2024 · Accepted: 30 January 2025 ·

Published Online: 25 February 2025



Wenjie Zhang (张文杰), Yuan Zhuang (庄园), Decheng Wan (万德成), and Jianhua Wang (王建华)^{a)}

AFFILIATIONS

Computational Marine Hydrodynamics Lab (CMHL), School of Ocean and Civil Engineering, Shanghai Jiao Tong University, Shanghai 200240, China

Note: This paper is part of the Special Topic, Wave-Structure Interaction.

^{a)} Author to whom correspondence should be addressed: jianhuawang@sjtu.edu.cn

ABSTRACT

Ship motions, local wave impact loads on ship bow and global wave-induced structural responses of a 20 000 TEU (twenty-foot equivalent unit) containership are studied in irregular and freak waves. A two-way coupled CFD-MBD (computational fluid dynamics–multi body dynamics) method is adopted for the co-simulation of the interactions between flow field and structure model of an elastic ship beam. The fluid–structure interaction method is validated with experimental measurement in regular waves. It is found that the maximum value of the vertical bending moment response amplitude operator appears in the condition of $\lambda/L = 1.0$. In the flow field, a potential-viscous flow coupled HOS-CFD (high order spectrum–CFD) method is applied in the simulation of the irregular and freak waves. The freak wave generated by HOS-CFD method shows good agreement with the HOS input data. It is found that the amplitude of pitch motion is most sensitive to the wave height of irregular waves. When the significant wave height of the irregular wave increases by 1.6 times, the VBM, heave, and pitch responses increase by about 2 times, 3.5 times, and 6 times, respectively. In addition, the cumulative distributions of hull motion, VBM amidship, and most sensor pressures are well fitted with Weibull distribution. In high sea states, bow slamming and green water are the main causes of high frequency responses of VBM.

Published under an exclusive license by AIP Publishing. <https://doi.org/10.1063/5.0254680>

I. INTRODUCTION

The prediction of ship motions and wave loads has been a great concern for the design and strength check of ship and ocean engineering structures. With the development tendency of ships becoming large-scale, light-weighted, and high-speed, the hydroelastic responses have been increasingly important, especially for the ships whose size exceeds the limits of the classification of society rules and experience, like 20 000 TEU containerships.¹ In addition, compared with the traditional prediction of seakeeping performance based on rigid hull models, the hydroelasticity study is helpful to simulate the ship motions, external wave loads, and the wave-induced internal forces at the same time, which can bring great benefit for ship design. Since the last century, many scholars have worked extensively in ship hydroelasticity studies, both by experimental measurements and numerical simulations.

In the early time of ship hydroelastic studies, the research methods are primarily based on model tests^{2–4} and numerical simulations with potential flow theory.^{5–7} With the development over the past few decades, both methods have gradually become mature analytical

means. Many of the earlier studies focused on the responses in regular waves. However, the actual sea conditions are more complex, which can be simplified with long-crested irregular waves, meaning the uncertainty of the responses and the analysis based on statistics methods. In recent years, some scholars have studied the ship hydroelastic problems in irregular waves. In the ship model experiments, Tang *et al.*⁸ have measured the vibrations, ship motions, and wave impact loads under different azimuth and wave height with trimaran model tests in oblique irregular waves. Hashimoto *et al.*⁹ have tested the wave-induced forces of ONR tumblehome ship in irregular stern quartering waves. Jiao *et al.*¹⁰ have studied the relations between VBM (vertical bending moment) and HBM (horizontal bending moment) of a large-scale segmented ship model in a seaway. Kim *et al.*¹¹ have studied the ship course keeping control and turning performance with a KCS ship model in irregular waves. Xie *et al.*¹² have summarized the hydroelastic responses of a barge and a KVLCC2 ship model in irregular head waves. In the numerical studies based on the potential flow theory, Chen *et al.*¹³ and Cheng *et al.*¹⁴ have numerically predicted the hydroelastic responses including vertical deformations and bending

moments of very large floating structure (VLFS) in oblique irregular waves, respectively. Chen *et al.*¹⁵ have studied the VBM, HBM, SBM (splitting bending moments), and TTM (transverse torsional moments) responses of a high-speed trimaran in oblique regular and irregular waves. Jiao *et al.*^{16,17} have systematically studied the responses of ship motions as well as VBM and HBM loads in head and oblique irregular waves with model tests and numerical simulations based on a three-dimensional time-domain nonlinear potential theory. In addition, the extreme design loads are determined, and an improved rule is proposed to evaluate the ultimate strength of hull structure based on the present classification society rule approaches. Jin *et al.*¹⁸ have numerically simulated the responses of vertical displacements and VBM loads of a coupled multi-floater-mooring system in regular and irregular waves. Michele *et al.*¹⁹ have studied the hydroelastic responses of vertical displacements of a floating circular plate in regular and irregular waves with experimental measurements and numerical simulations based on linear potential flow theory. On the whole, the numerical predictions based on the potential flow theory can be effectively applied in the studies of ship hydroelasticity. However, it is limited in the simulations of wave breaking, green water, and solutions of local wave-induced loads, which can be effectively solved based on CFD method.

In recent years, many scholars have combined the CFD method with different structural simulation methods, such as FEM method (finite element method),^{20–22} MBD method,^{23–26} and so on. The combination of the FSI (fluid–structure interaction) simulation model is then applied in the numerical simulations of ship hydroelasticity. Many researchers^{23–26} have applied the CFD solver, OpenFOAM, and the structural dynamic solver, MBDyn with the self-developed FSI coupling tool or open-source FSI coupling library, preCICE to form the ship hydroelastic solver. Liu *et al.*²³ have adopted the hydroelastic solver in the study of the impact of blade elasticity and influence of platform surge motion in the co-simulation between a floating offshore wind turbine (FOWT) and constant wind. Wei *et al.*^{24,25} have studied the ship hydroelastic responses of the intact and damaged hull structures of the S-175 container ship model under regular head waves. Zhang *et al.*²⁶ have compared the VBM responses in regular waves with different wavelengths and the responses of elastic and rigid ship body structures. However, the relevant work mainly focuses on the studies in regular waves, and the studies in irregular waves are relatively rare. Li *et al.*²⁷ have studied the nonlinear wave-body interactions for a stationary floating structure in regular and irregular waves in a two-dimensional numerical wave tank without considering the influence of hydroelasticity. Hashimoto *et al.*⁹ have numerically simulated the wave-impact loads on ships in irregular stern quartering seas with the in-house code CFDShip-Iowa and validated the results with experimental data. Jiao *et al.*²⁸ have numerically predicted the ship motions and external loads of a rigid S-175 containership model in cross waves. Huang *et al.*²⁹ have studied the hydroelastic responses of the heave and pitch motions and VBM loads of a single module VLFS in regular and freak waves. Xie *et al.*¹² have calculated the hydroelastic responses of a barge and a KVLCC2 ship with a business software LS-DYNA. The numerical predictions are also validated with the model test data. However, on the whole, the CFD method is rarely applied to predict the ship hydroelasticity in irregular waves, and one of the main reasons is the expensive computational cost, especially for the long-time simulation of irregular waves. One of the effective methods to

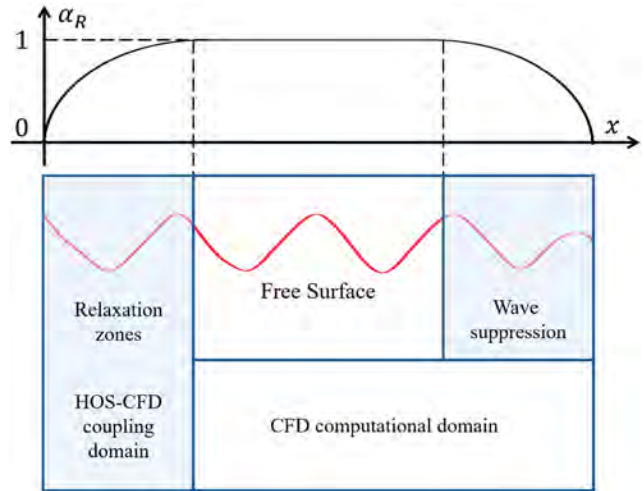


FIG. 1. Weight coefficient α_R in relaxation zones.

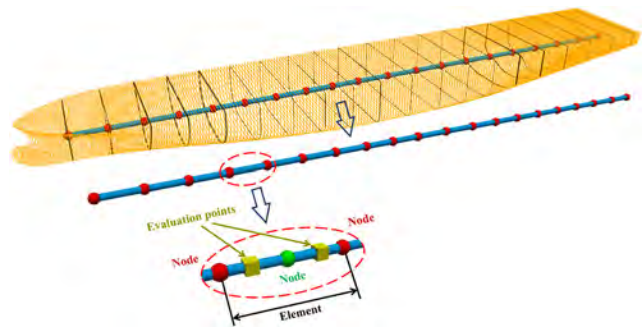


FIG. 2. Three-node beam model in MBDyn.

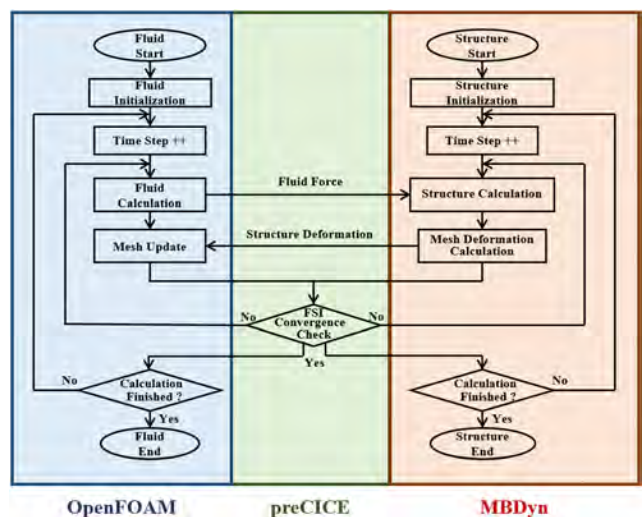


FIG. 3. Numerical framework of the FSI coupling.

balance high accuracy and relative high efficiency is to compute the fluid field with both the potential flow theory and the CFD method, such as the coupling HOS-CFD (high order spectrum-CFD) method adopted in this study. First, the HOS method is applied to generate the irregular waves with large domain and long time. Then the HOS results are interpolated to CFD domain on the inlet boundary and relaxation zone (the details seen in Sec. II A). In this way, the computational cost can be limited as accepted with relative small domain and the specified time series of wave height, which can be checked before the co-simulations of FSI. It balances the advantages of high accuracy of CFD simulation and high efficiency with the potential flow theory. The coupled HOS-CFD-MBD method is adopted in the numerical predictions of ship motions and wave loads in irregular and freak waves in this study. It filled the gap on the application of HOS-CFD-MBD method to predict ship hydroelasticity in irregular and freak waves with relative high efficiency and high accuracy.

In the present work, a coupled HOS-CFD-MBD method is adopted to the numerical prediction of motion and hydroelastic performance of a 20 000 TEU containership in irregular and freak waves. For the FSI simulations of regular waves, the fluid field is solved with CFD method by the wave making tool of waves2Foam. For the simulations of irregular and freak waves, the flow fluid field is calculated with potential-viscous coupling HOS-CFD method. The waves are first generated by HOS method and then transferred to CFD zone, which is solved by OpenFOAM, and the structural responses are calculated with open source toolbox MBDyn. The data exchange between HOS solver and CFD solver is based on the open-source tool of grid2Grid, and the interpolation and projection of FSI procedure is achieved by preCICE. The predictions of ship motions and VBM load in regular waves are validated with the available experimental data. The ship hydroelastic responses in irregular and freak waves are discussed in detail.

TABLE I. Principal particulars of the 20 000 TEU containership.

Items	Symbol	Full scale	Model scale
Scale	μ	1:1	1:49
Length between perpendiculars	L_{pp} (m)	383.0	7.816
Breadth	B(m)	58.6	1.196
Depth	D (m)	30.5	0.622
Fore draught	d_F (m)	15.2	0.310
After draught	d_A (m)	16.7	0.341
Displacement	Δ (t)	2.58×10^5	2.161
Block coefficient	C_B	0.69	0.69
Center of gravity longitudinal center of gravity (LCG) from aft perpendicular (AP)	X_g (m)	182.7	3.729
Vertical center of gravity (KG) from baseline	Z_g (m)	27.6	0.563
Moment of inertia about y-axis	I_{yy} (kg m ²)	2.307×10^{12}	7967.86



FIG. 4. A 3D view of the model hull.

II. NUMERICAL APPROACHES

In this study, a two-way coupled CFD-MBD method is adopted in the numerical predictions of ship motions and structural responses of a 20 000 TEU containership in head waves. In addition, the coupling HOS-CFD method is applied in the simulations of irregular and freak waves. The fluid part is solved by the open-source libraries of HOS-NWT³⁰ and OpenFOAM, and the solid domain is calculated by MBDyn. The coupling data of fluid pressure and structure deformations are interpolated and projected with the help of preCICE. The details of the FSI coupling procedures are described below.

A. Fluid simulation method

In the numerical simulations of flow field, the coupled HOS-CFD method is applied to generate the irregular and freak waves. The HOS method with high efficiency and accuracy has been widely used for the wave generations with large computational domain and long-time duration.^{31–34} The HOS method is based on the partial difference equations (PDEs) on kinematic and dynamic free surface boundary conditions,³¹

$$\eta + \nabla_x \phi^s \cdot \nabla_x \eta - (1 + \nabla_x \eta \cdot \nabla_x \eta) \phi_z(\mathbf{x}, \eta, t) = 0, \quad (1)$$

$$\phi^s + g\eta + \frac{1}{2} \nabla_x \phi^s \cdot \nabla_x \phi^s - \frac{1}{2} (1 + \nabla_x \eta \cdot \nabla_x \eta) \phi_z^2(\mathbf{x}, \eta, t) = -P_a, \quad (2)$$

where ϕ and ϕ^s are the velocity potential and surface velocity potential, respectively. t denotes time, \mathbf{x} denotes position, and g denotes the acceleration caused by gravity. η is the wave surface elevation function about t and \mathbf{x} . $\nabla_x \equiv \left(\frac{\partial}{\partial x}, \frac{\partial}{\partial y} \right)$ is the slope in the horizontal direction, and P_a denotes atmospheric pressure. The surface velocity potential $\phi^s(\mathbf{x}, t)$ is able to be written as a perturbation series and further expanded with Taylor series,³¹

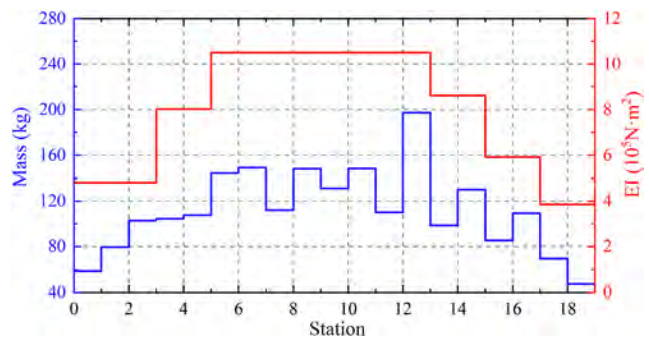


FIG. 5. Longitudinal mass and vertical bending stiffness distributions of the ship beam.

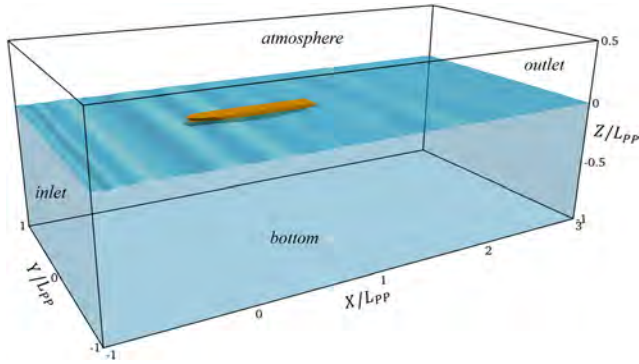


FIG. 6. General view of the computational domain.

$$\phi^s(\mathbf{x}, t) = \sum_{m=1}^M \sum_{k=0}^{M-m} \frac{\eta^k}{k!} \frac{\partial^k}{\partial z^k} \phi^{(m)}(\mathbf{x}, 0, t). \quad (3)$$

Furthermore, the velocity potential in the horizontal and vertical directions are given by Refs. 31 and 32, respectively,

$$\phi^{(m)}(\mathbf{x}, 0, t) = - \sum_{k=1}^{m-1} \frac{\eta^k}{k!} \frac{\partial^k}{\partial z^k} \phi^{(m-k)}(\mathbf{x}, 0, t), \quad m = 2, 3, \dots, M, \quad (4)$$

$$\phi_z^{(m)}(\mathbf{x}, \eta, t) = \sum_{k=0}^{m-1} \frac{\eta^k}{k!} \frac{\partial^{k+1}}{\partial z^{k+1}} \phi^{(m-k)}(\mathbf{x}, 0, t). \quad (5)$$

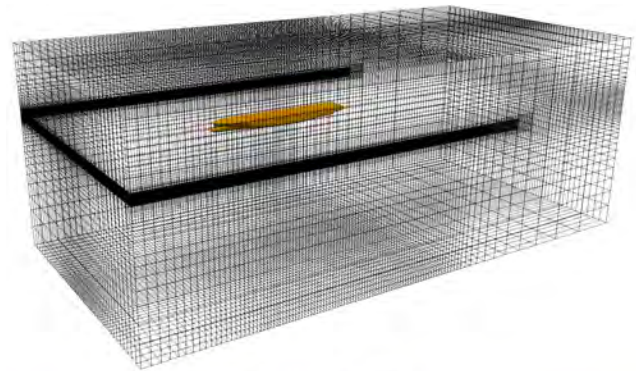
With the initial conditions known in the simulation, Eqs. (3)–(5) can be solved. More details can be found in the work of Zhuang *et al.*³⁵ In addition, the fourth-order Runge-Kutta method is adopted in the time step iterations in HOS computational domain.

As for the CFD domain, the fluid field of two-phase, incompressible and unsteady flow is governed by the continuity and Navier-Stokes equations as

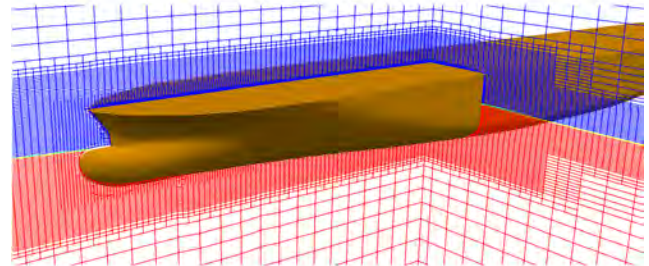
$$\nabla \cdot \mathbf{U} = 0, \quad (6)$$

$$\frac{\partial(\rho \mathbf{U})}{\partial t} + \nabla \cdot (\rho \mathbf{U} \mathbf{U}) = -\nabla p + \nabla^2(\rho \mu \mathbf{U}) + \rho \mathbf{g}, \quad (7)$$

where \mathbf{U} , p , and \mathbf{g} means flow velocity, fluid pressure, and acceleration due to gravity, respectively. The fluid density, ρ , and the kinematic



(a) General 3D view



(b) Refinement details around ship hull

FIG. 7. Computational mesh distribution.

viscosity, μ , are determined by the volume of fluid (VOF) method to capture the free surface between water and air³⁶ with the equation as

$$\frac{\partial \alpha}{\partial t} + \nabla \cdot (\alpha \mathbf{U}) + \nabla \cdot [\alpha(1 - \alpha) \mathbf{U}_r] = 0, \quad (8)$$

where α denotes the proportion of water in the grid. The proportion α is limited between 0 and 1, representing the mesh cell filled with air and water, respectively. \mathbf{U}_r is the velocity vector for the interface compression. The two-equation $k - w$ shear stress transport (SST) turbulence model is adopted to solve the continuity and momentum equations. More details can be found in the work of Menter.³⁷ The PIMPLE algorithm (combination of PISO and SIMPLE algorithms) is applied to decouple the relations between velocity and pressure. In addition, the schemes of Euler, total variational diminishing (TVD),

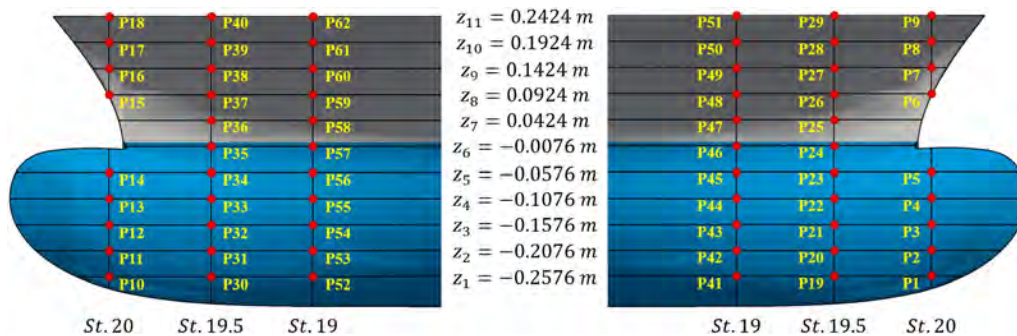


FIG. 8. Arrangement of pressure sensors on portboard (left) and starboard (right).

TABLE II. Calibrated beam natural frequency of model vertical bending modes.

Order	Mode	f_{MBD} (Hz)	f_{exp} (Hz)	Error (%)
First	2-node	3.87	3.82	1.20
Second	3-node	8.82	8.57	2.88

and central differential are applied in the computation of temporal, convection, and diffusion terms, respectively.

The combination between HOS domain and CFD domain is based on the relaxation zones by using open source libraries of Grid2Grid³⁸ and waves2Foam.³⁹ The Grid2Grid reconstructs the wave field of HOS by inverse fast Fourier transforms (IFFT) and makes it interpolated with the method of fast spline interpolation. In this way, the frequency-domain results calculated by HOS are converted into time-domain results and interpolated to the center point of the CFD grids to update physical quantities such as velocity, pressure, and water proportion. The waves2Foam provides a useful tool of relaxation zones for wave generation and interpolation in CFD field from HOS computational domain. In the relaxation zones, the physical parameter ϕ (including pressure, velocity, etc.) can be expressed as

$$\phi = (1 - \alpha_R)\phi_{target} + \alpha_R\phi_{computed}, \quad (9)$$

where the weight coefficient α_R is limited to 0 and 1, and ϕ_{target} and $\phi_{computed}$ represent the HOS and CFD solutions, respectively. The distribution of α_R in the relaxation zone is shown in Fig. 1. The wave damping in the outlet relaxation zone is realized with numerical suppression to avoid wave reflections. More information of the HOS-CFD coupling method can be referred to Zhuang *et al.*³⁵

The irregular wave in this study is numerically created based on the JONSWAP wave spectrum with the non-dimensional peak shape parameter $\gamma = 3.3$. The JONSWAP wave spectrum can be described as⁴⁰

$$S(\omega) = \alpha S_{PM}(\omega) \gamma \exp\left[-\frac{(\omega/\omega_p - 1)^2}{2\sigma^2}\right], \quad (10)$$

where $S_{PM}(\omega)$ is the Bretschneider or two-parameter Pierson-Moskowitz spectrum, which is expressed as

$$S_{PM}(\omega) = \frac{5}{16} H_s^2 \left(\frac{2\pi}{T_p}\right)^4 \omega^{-5} \exp\left[-\frac{5}{4} \left(\frac{2\pi}{T_p}\right)^4 \omega^{-4}\right], \quad (11)$$

where H_s , ω , ω_p , and T_p represent the significant wave height, the angular wave frequency, the peak angular frequency, and the peak wave period, respectively. α is the normalizing factor, and calculated as

TABLE III. Case parameters of different mesh levels.

Grid level	Cell number ($\times 10^6$)	Time step (s)	Solving time (h)
Coarse	3.08	0.001	32
Medium	4.31	0.001	47
Fine	6.17	0.001	67

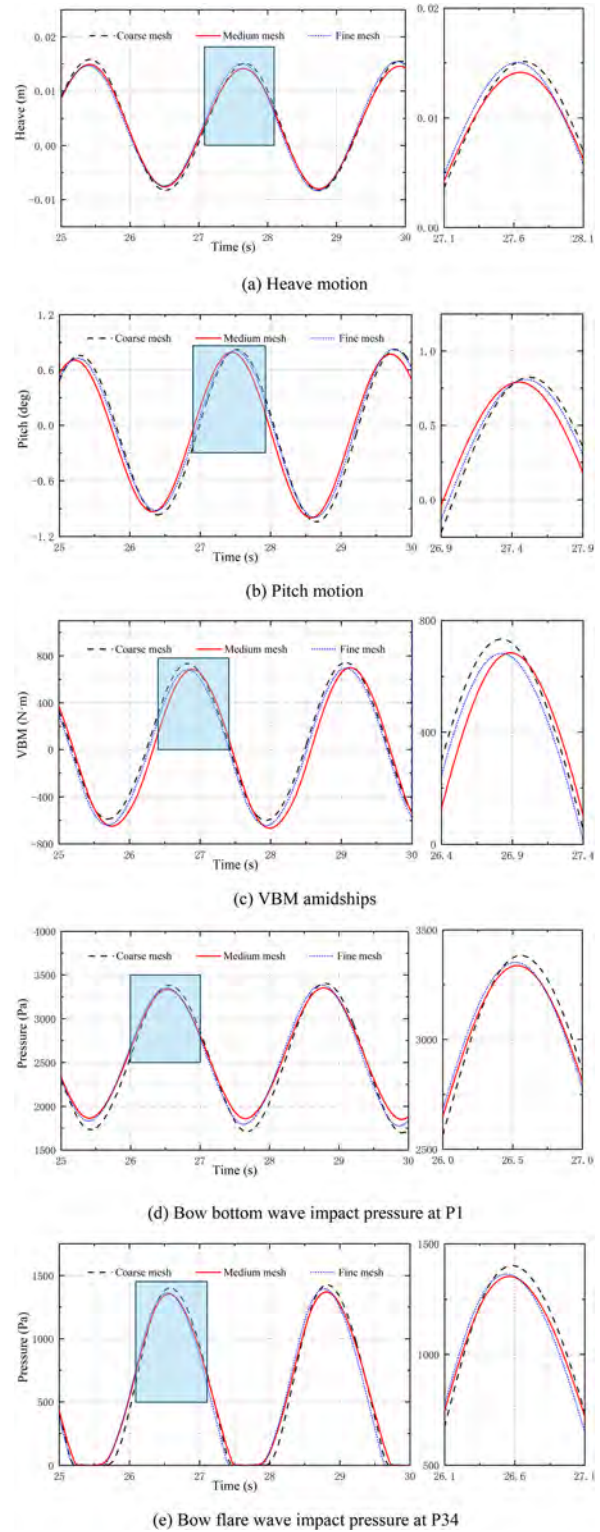


FIG. 9. Comparison of time histories of ship motions and loads of different mesh schemes.

TABLE IV. Results of convergence study of different grid levels.

Parameters		Crest value			Peak value	
Description	Symbol	Heave (mm)	Pitch (deg)	VBM (Nm)	P1 (Pa)	P34 (Pa)
Fine mesh	S_1	15.0	0.806	680.9	3351.3	1364.0
Medium mesh	S_2	14.1	0.786	683.9	3335.3	1352.9
Coarse mesh	S_3	15.1	0.823	733.2	3383.6	1402.9
Convergence rate	R	-0.85	-0.54	0.06	-0.33	-0.22
Convergence type	...	OC	OC	MC	OC	OC
Precision	P	0.47	1.83	8.32	3.28	4.47
Extrapolated values	$S_{ext,32}$	8.06	0.74	680.71	3311.37	1338.63
Approximate relative error	$e_{a,32}$	7.30%	4.71%	7.21%	1.45%	3.70%
Extrapolated relative error	$e_{ext,32}$	75.00%	5.86%	0.47%	0.72%	1.07%
Grid convergence index	GCI	0.54	0.07	0.01	0.01	0.01

$$\alpha = \frac{1}{5(0.1160 + 0.0594\sqrt{\gamma} + 0.0246\gamma)}. \quad (12)$$

The parameter of σ is specified as

$$\sigma = \begin{cases} 0.07, & \text{for } \omega/\omega_p \leq 1 \\ 0.09, & \text{for } \omega/\omega_p > 1. \end{cases} \quad (13)$$

In addition, the relationship between the mean wave period T_{0m1} and the peak wave period T_p can be evaluated as

$$T_{0m1} = (0.7757 + 0.0965\sqrt{\gamma} - 0.0144\gamma)T_p. \quad (14)$$

Because a two-way coupling of FSI is simulated in this study, a dynamic mesh motion solver displacement Laplacian is applied to update the fluid mesh. The coordinates of internal grids are calculated by solving the following Laplacian's equation:

$$\nabla \cdot (\gamma \nabla (\delta X)) = 0, \quad (15)$$

where γ denotes a diffusion coefficient as a constraint to increase the solution smoothness. The δX is the displacement field. In this study, a quadratic function of the inverse distance from the boundary is adopted, meaning $\gamma = 1/r^2$, and r is the distance from internal cell centers to structural boundaries.

B. Structure simulation method

In the present study, a simplified one-dimensional ship beam model is applied in the numerical predictions of ship motions and structural responses of the 20 000 TEU containership. The ship beam is discretized as different elements with the longitudinal mass and

TABLE V. Case parameters of different time step levels.

Time step level	Cell number ($\times 10^6$)	Time step (s)	Solving time (h)
Large	4.31	0.0014	37
Medium	4.31	0.001	47
Small	4.31	0.0007	62

stiffness distributions of the hull. The displacements of each node and the internal structural responses of evaluation points (yellow blocks in Fig. 2) on the ship beam are calculated with two degrees of freedom (heave and pitch motion degrees).

The structural dynamic responses are calculated with the open-source code, MBDyn, by solving Newton-Euler equations for each node in the ship beam.⁴¹ The governing equations with a Lagrange multiplier λ used to impose constraints are written in differential-algebraic form as^{42,43}

$$M\dot{\mathbf{x}} = \mathbf{q}, \quad (16)$$

$$\dot{\mathbf{q}} + \frac{\partial \phi}{\partial \mathbf{x}} \lambda = \mathbf{f}(\mathbf{x}, \dot{\mathbf{x}}, t), \quad (17)$$

$$\phi(\mathbf{x}, t) = 0, \quad (18)$$

where M and \mathbf{x} donate the inertial matrix of the rigid body and the kinematic variables in global system. Here, \mathbf{q} is the momentum and momenta moments vector, and $\phi(\mathbf{x}, t)$ represents a set of kinematic constraints applied to the body. The $\mathbf{f}(\mathbf{x}, \dot{\mathbf{x}}, t)$ denotes the external force and moment.

A geometrically non-linear three-node beam model is discretized with the finite volume approach.⁴⁴ As illustrated in Fig. 2, the hull girder is discretized as different elements by ship nodes of red circles. The internal node of green circle is always positioned at the midpoint of two outer nodes with red circles. In addition, both yellow blocks are set in the Gauss points of the element, from where the internal shear forces and bending moments are computed.

The positioning of the ship model is also set in the structural solver. In the present work, only the ship motions in head waves and the symmetry structural responses are concerned. Therefore, only the motions of heave and pitch are set free for each node on the ship beam.

C. FSI coupling method

The FSI coupling between fluid solver and structure solver is based on an open-source library, preCICE, which provides an effective and high-efficient platform for the communications of data interpolation and projection. The computations of both fluid and solid parts will repeat for several times in each time step to realize the strong

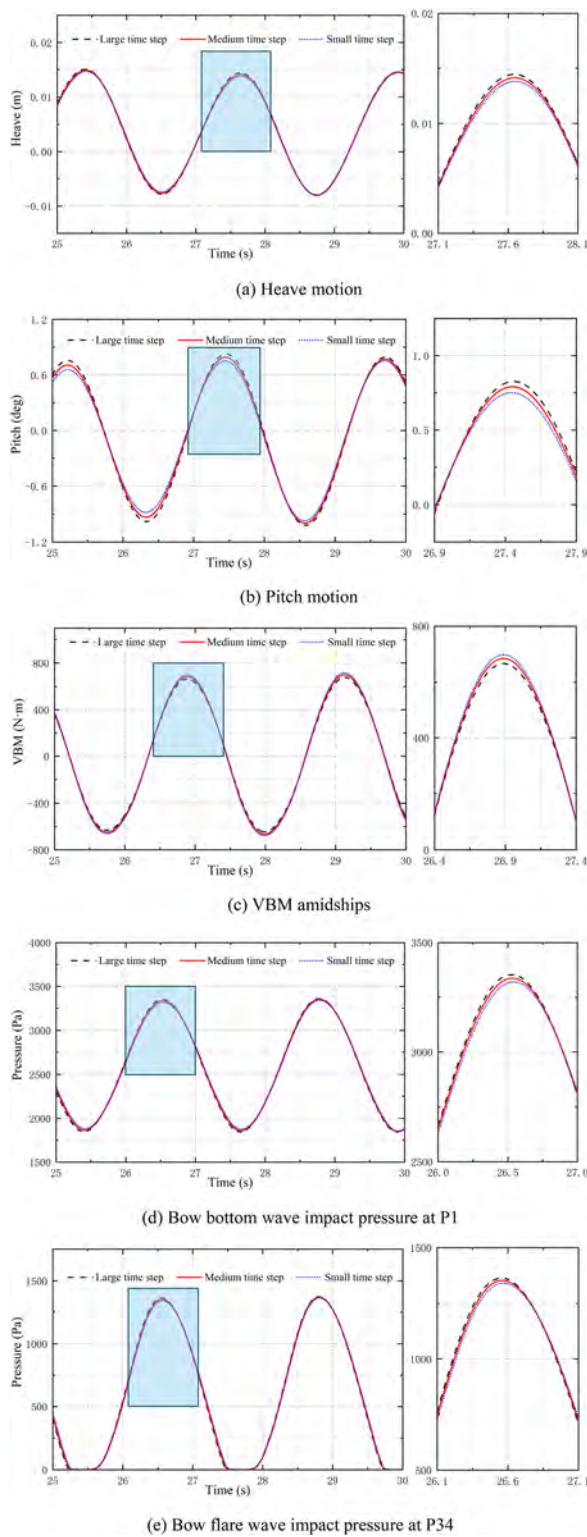


FIG. 10. Comparison of time histories of ship motions and loads of different time step schemes.

coupling algorithm. The computational mesh of fluid field will be updated after obtaining the information about structural deformation to realize the two-way coupling algorithm. The framework of FSI coupling procedure is shown in Fig. 3.

In Fig. 3, the numerical simulations of FSI procedure start from the initializations of both fluid and structure solvers. In each time step, the flow field is first solved to obtain the fluid pressure, which is then transformed into the solid solver to calculate structural responses of ship beam. The structural deformations are interpolated and projected back to the computational meshes of fluid domain. The fluid field is then solved again after the update of mesh, which will start a new iteration loop until the residuals of both fluid pressure and solid deformation satisfy the limited value. The two-way coupling with preCICE has been validated as high accuracy.⁴⁵ In addition, the coupling strategy has also been validated in the prediction of ship hydroelasticity in regular waves.²⁶ The present paper extends the method from CFD-MBD to HOS-CFD-MBD and also make it possible to simulate the hydroelastic responses in irregular waves and freak waves.

III. GEOMETRY AND COMPUTATIONAL SETUPS

A. Ship model description

This section describes the geometry of the 20 000 TEU container-ship model with the scale ratio of 1:49. The numerical simulations are based on the bare hull model without any appendages. The main dimensions and a general 3D view of the containership model are given in Table I and Fig. 4, respectively.

The longitudinal mass and vertical bending stiffness distributions of the hull girder is shown in Fig. 5. The ship beams in the experiments of CSSRC (China Ship Scientific Research Center) are constructed by assembling six circular tubes with different cross-sectional sizes, making the distributions of vertical bending stiffness composed of six distinct segments. The ship beam is divided into 19 elements based on the position of the stations. In addition, the damping ratio of the structural beam model is set as zero in the numerical simulations, which is consistent with the approach taken by Jiao *et al.*⁴⁶

B. Computational setup

Figure 6 shows a general view of the computational domain of the fluid field with the extent of $-1L_{pp} < x < 3L_{pp}$, $-1L_{pp} < y < 1L_{pp}$, and $-1L_{pp} < z < 0.5L_{pp}$. The relaxation zone of wave making inlet domain starts from $-1L_{pp}$ and ends at $-0.5L_{pp}$ in the longitudinal direction. The sponge zone of wave suppression outlet region starts from $2L_{pp}$ and ends at $3L_{pp}$. The Stokes first-order wave is generated by velocity inlet boundary conditions.⁴⁷ The velocity conditions of inlet and outlet boundaries are set as zero gradient. The pressure boundary conditions of inlet and outlet are specified as zero flux pressure and zero gradient, respectively. The bottom boundary and hull surface are defined as wall and moving wall boundary conditions, respectively. The left and right boundaries are set as symmetry plane. The top region of the domain is specified as atmosphere with zero pressure and computed velocity.

The computational domain of flow field is discretized and refined locally at the positions of free surface and ship body with the pre-processing tools of blockMesh and snappyHexMesh in OpenFOAM, as illustrated in Fig. 7. The refinement of computational mesh satisfies the criterion of 12 cells per wave height and over 120 cells per wavelength for the simulation condition of $\lambda/L = 1.0$. The ratio of grid

TABLE VI. Results of convergence study of different time step levels.

Parameters		Crest values			Peak values	
Description	Symbol	Heave (mm)	Pitch (deg)	VBM (Nm)	P1 (Pa)	P34 (Pa)
Small time step	S_1	13.8	0.752	697.5	3319.9	1341.8
Medium time step	S_2	14.1	0.786	683.9	3335.3	1352.9
Large time step	S_3	14.5	0.827	665.1	3353.6	1364.3
Convergence rate	R	0.75	0.83	0.72	0.84	0.97
Convergence type	...	MC	MC	MC	MC	MC
Precision	P	0.85	0.56	0.96	0.51	0.08
Extrapolated values	$S_{ext,32}$	12.90	0.59	733.07	3238.12	931.10
Approximate relative error	$e_{a,32}$	2.84%	5.22%	2.75%	0.55%	0.84%
Extrapolated relative error	$e_{ext,32}$	9.30%	33.93%	6.71%	3.00%	45.30%
Time step convergence index	GCI	0.11	0.32	0.09	0.04	0.39

height to grid length in the refinement regions around hull surface is set as 1:2 to accurately capture the hull geometry. The ratio of grid height to length in other computational regions on the free surface is maintained as 1:4 for the accurate simulation of the regular and irregular waves. The total mesh number in this study is 4.31×10^6 . In order to study the wave impact interactions on ship bow, a number of pressure sensors are arranged symmetrically on the portboard and starboard, as illustrated in Fig. 8.

IV. NUMERICAL VALIDATIONS

A. Modal analysis

In hydroelasticity studies, since the structural responses are solved by the ship beam model, it is crucial to validate the distributions of mass and stiffness through modal analysis. This validation involves calculating and comparing the two-node and three-node natural frequencies with experimental measurements. The LAPACK solver in MBDyn is utilized for the modal analysis. The computed natural

frequencies exhibit good agreement with the experimental data, as shown in Table II.

B. Convergence study

In this section, the convergence studies of flow field grid and time step are involved to check the uncertainties in the numerical simulations. All the cases in the convergence studies are under the condition of $\lambda/L = 1.0$ with zero ship speed. Table III shows the details of different grid schemes.

The Richardson extrapolation method is adopted in the convergence check to calculate the convergence rate R , computational precision P , extrapolated value S_{ext} , approximate relative error e_a , extrapolated relative error e_{ext} , and the GCI (grid convergence index) as follows:

$$R = \frac{s_2 - s_1}{s_3 - s_2} = \frac{\epsilon_{21}}{\epsilon_{32}}, \tag{19}$$

$$P = \frac{\left| \ln \left| \frac{\epsilon_{21}}{\epsilon_{32}} \right| \right|}{\ln r}, \tag{20}$$

$$S_{ext,32} = \frac{r^P s_2 - s_3}{r^P - 1}, \tag{21}$$

$$e_{a,32} = \frac{|s_3 - s_2|}{|s_2|}, \tag{22}$$

$$e_{ext,32} = \frac{|s_{ext,32} - s_2|}{|s_{ext,32}|}, \tag{23}$$

$$GCI = \frac{1.25 \times e_{a,32}}{r^P - 1}, \tag{24}$$

where s_1 , s_2 , and s_3 represent the numerical predictions of ship motions, VBM load amidship and wave impact loads on ship bow with fine mesh (or small time step), medium mesh (or medium time step), and coarse mesh (or large time step), respectively. $S_{ext,32}$, $e_{a,32}$, and $e_{ext,32}$ are the extrapolated value, approximate relative error, and extrapolated relative error based on s_2 and s_3 , respectively. According to the value of convergence ratio R , there can be four types of convergence modes of monotonic convergence (MC) ($0 < R < 1$), oscillatory convergence (OC) ($-1 < R < 0$), monotonic divergence (MD) ($1 < R$), and oscillatory divergence (OD) ($R < -1$).

TABLE VII. Details of validation conditions.

Case ID	Wavelength (λ/L)	Wave frequency (ω , rad/s)	Wave steepness (H/λ)
V1	0.6	3.625	0.0218
V2	0.7	3.356	0.0186
V3	0.8	3.140	0.0163
V4	0.9	2.960	0.0145
V5	1.0	2.808	0.0131
V6	1.1	2.678	0.0119
V7	1.2	2.564	0.0109
V8	1.3	2.463	0.0100
V9	1.4	2.373	0.0093
V10	1.5	2.293	0.0087
V11	1.6	2.220	0.0082
V12	1.8	2.093	0.0073
V13	2.0	1.986	0.0065
V14	2.5	1.776	0.0052

25 February 2025 14:44:23

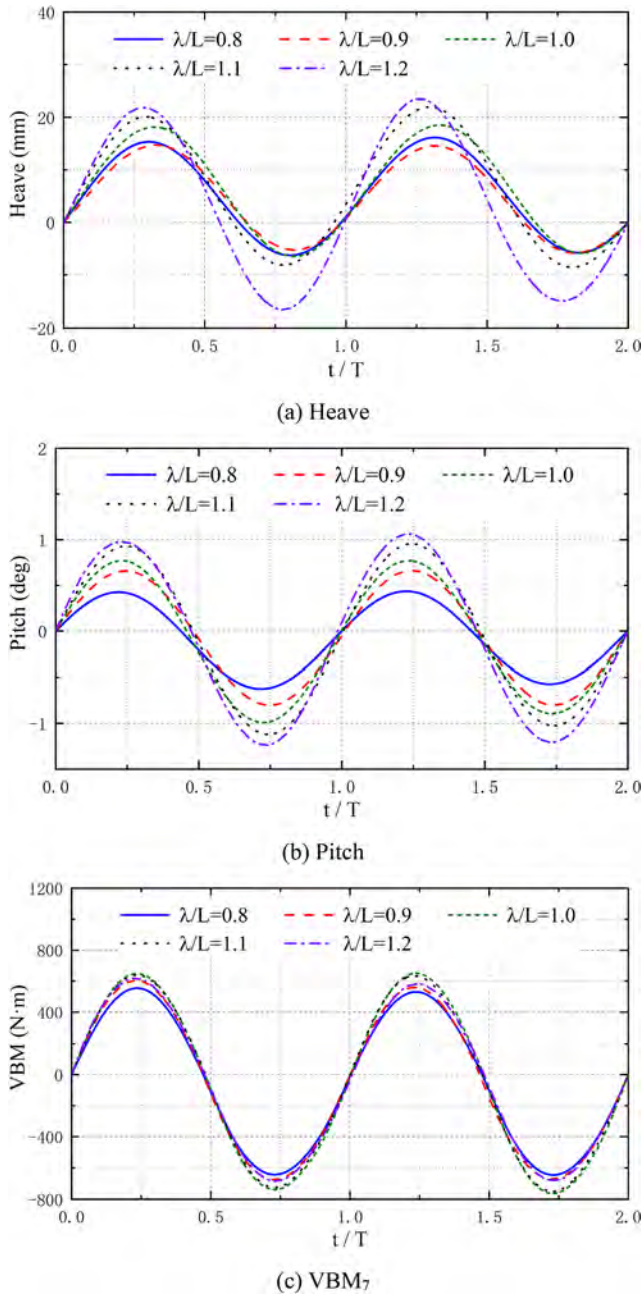


FIG. 11. Comparison of time series of ship motion and VBM amidship.

The time series of ship motions, VBM load amidships, and wave impact pressure at P1 and P34 on ship bow are illustrated in Fig. 9. It is seen that the time histories of ship motions and loads show high degrees of consistency and the tendency of monotonic convergence. The convergence study results for different grid schemes are summarized in Table IV. It is seen that monotonic convergence is obtained for all the variables concerned. All of the three grid schemes show good consistency, and the medium-sized mesh is chosen for the

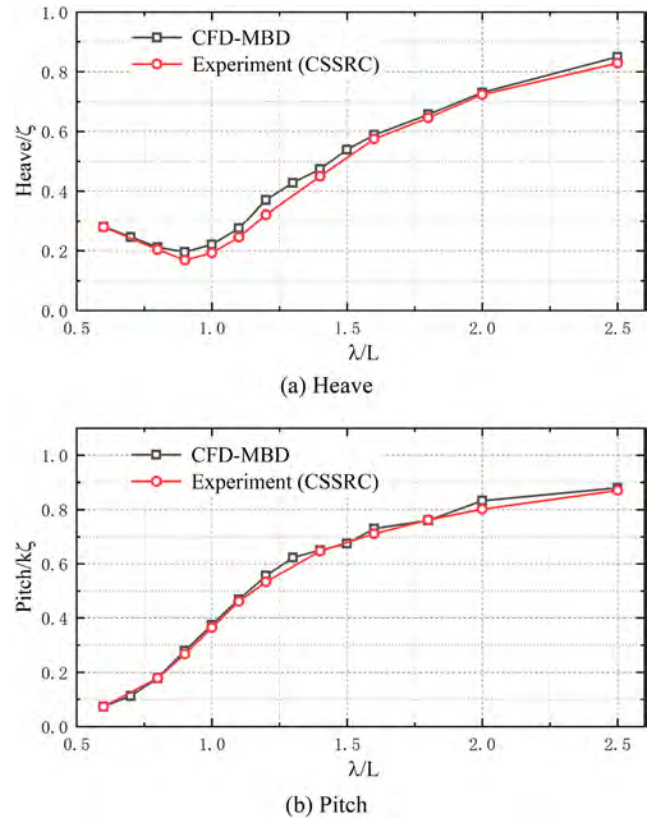


FIG. 12. Comparisons of RAOs of ship motions.

further studies with the consideration of computational accuracy and efficiency.

The convergence analysis of time step is conducted similarly. The details of different time step schemes are summarized in Table V. The numerical predictions of ship motions of heave and pitch, VBM load amidship, wave impact pressure at P1 and P8 sensors are illustrated in Fig. 10. The convergence results are shown in Table VI. The time series and statistical data of ship motions and loads show good consistency and monotonic convergence. The medium time step is chosen in the following simulations as a compromise between computational accuracy and efficiency.

C. Experimental validation

In this section, a series of validation conditions are numerically computed for the comparison with experimental measurements from CSSRC, as listed in Table VII. All the cases are simulated in regular head waves with a wave height of 102 mm (5 m in full scale) and zero ship speed. More validation results can be seen in Zhang *et al.*²⁶ The time histories of ship motion and VBM load amidship with different wavelengths are compared in Fig. 11.

The comparisons of non-dimensionalized motion and VBM results are illustrated in Figs. 12 and 13. The details of the RAO (response amplitude operator) statistics are shown in Tables VIII and IX. The numerical predictions show good agreement with

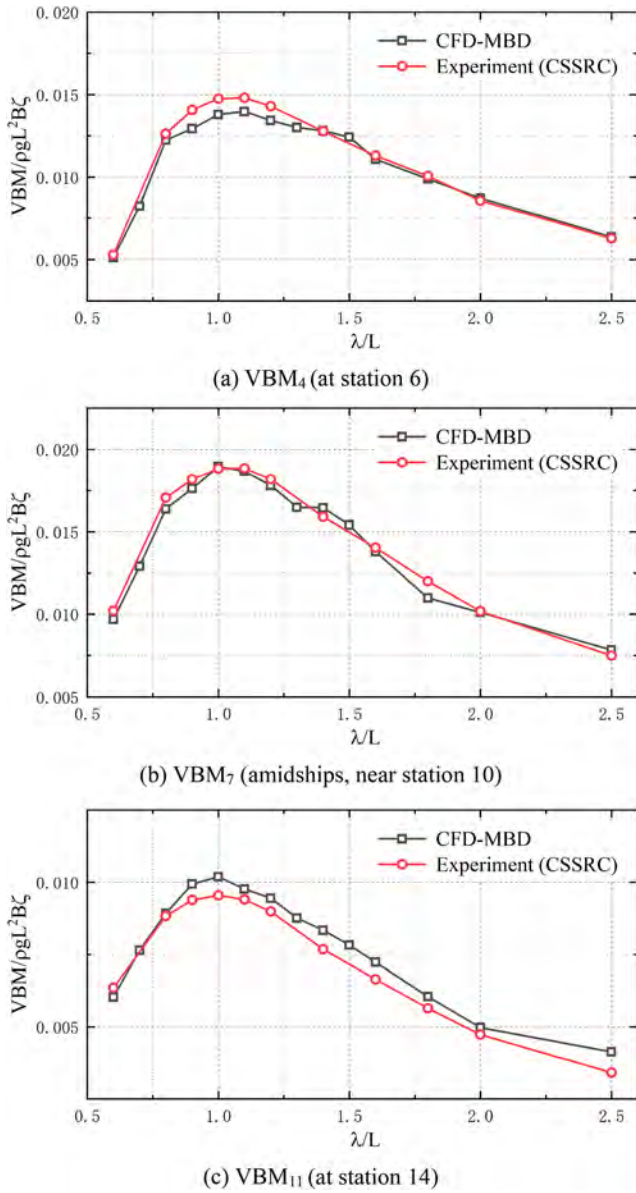


FIG. 13. Comparisons of RAOs of VBM loads.

experimental data with the same tendency and similar RAO values. As for the VBM comparison, the results at three different profiles are summarized, where the detailed locations are able to be found in the work of Si *et al.*⁴⁸

It is noticed from the comparisons of the RAOs of ship motions and VBM loads with different wavelengths that the amplitude of heave motion reaches the minimum value in the condition of $\lambda/L = 0.9$. While the VBM response obtains its maximum value of the amplitude with the condition of $\lambda/L = 1.0$. As for the pitch motion, there is a significant monotonically increasing relation between the RAO of pitch motion and the wavelength.

TABLE VIII. Summaries of RAOs of ship motions.

Wavelength (λ/L)	Heave/ ζ			Pitch/ $(k\zeta)$		
	CFD	EFD	Error (%)	CFD	EFD	Error (%)
0.6	0.281	0.280	0.5	0.074	0.073	1.4
0.8	0.212	0.204	4.2	0.179	0.179	-0.2
0.9	0.196	0.169	15.9	0.279	0.267	4.6
1.0	0.221	0.193	14.6	0.375	0.365	2.7
1.1	0.276	0.246	12.3	0.469	0.461	1.6
1.2	0.371	0.321	15.4	0.556	0.534	4.2
1.4	0.474	0.450	5.3	0.651	0.647	0.6
1.6	0.588	0.575	2.3	0.730	0.711	2.7
1.8	0.657	0.646	1.7	0.760	0.762	-0.2
2.0	0.730	0.723	1.0	0.833	0.802	3.9
2.5	0.850	0.829	2.6	0.880	0.871	1.1

V. RESULTS AND DISCUSSION

A. Responses in irregular wave

In the simulation of irregular waves, the time history of wave in 600 s is first calculated by HOS-NWT code. The computation is based on the JONSWAP spectrum with the significant wave height as 0.102 and 0.265 m in model scale, as shown in Table X. The irregular wave conditions are simulated based on the high-performance computing platform (Siyuan-1) of Shanghai Jiao Tong University by using one CPU node (Intel Xeon ICX Platinum 8358) with 64 cores. The peak time is determined with the recommendation of IACS (International Association of Classification Societies) (2022). The wave data of HOS results from 100 to 400 s are set as input into the wave generation domain of CFD computation. In addition, there is a region of $0.5 L_{pp}$ long left for the development of the irregular waves before the interactions with ship model. Figures 14 and 15 show the time series of wave elevations and the comparison between numerical and theoretical spectrum, respectively. With the statistics of the time series, there are 178 and 102 sub-wave components in the 300 s time interval for case I and case II, respectively. The significant values of wave height are 0.096 and 0.265 m for case I and case II, with the relative error of 5.88% and 0.04%, respectively. The maximum, significant, and average values of wave height are listed in Table XI. It shows that the significant wave height is about 1.6 times the average one, which accords with the general cognition. The relation between the maximum wave height and the significant one shows good agreement with the summary of Divinsky *et al.*⁴⁹ based on experimental measurements.

As seen in Fig. 15, most sub-wave components in main frequency ranges can be effectively simulated with HOS-CFD method. However, the wave components with small periods and small wavelength are less captured, which may be related to the limitation of mesh refinement and the dissipation of small waves. Figure 16 illustrates the time histories of the responses of ship motion and VBM amidship. The comparison of the response amplitudes in irregular waves with different wave height are summarized in Table XII. It is noticed that the significant wave height of case II is 1.6 times larger than case I, and the VBM response of case II is about three times that of case I. The difference of

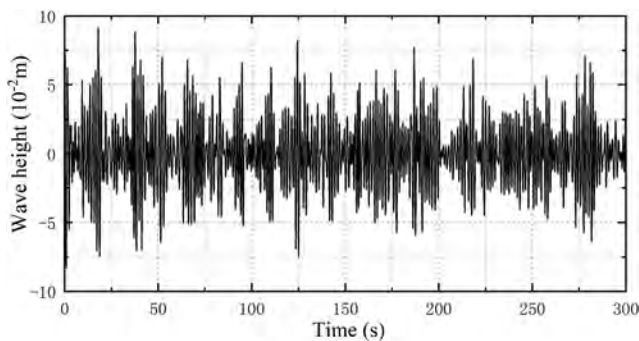
25 February 2025 14:44:23

TABLE IX. Summaries of RAOs of VBM loads.

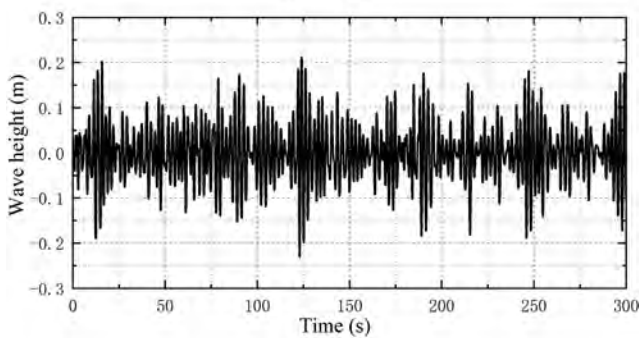
Wavelength (λ/L)	VBM ₄ / $(\rho\zeta gL^2B)$			VBM ₇ / $(\rho\zeta gL^2B)$			VBM ₁₁ / $(\rho\zeta gL^2B)$		
	CFD	EFD	Error (%)	CFD	EFD	Error (%)	CFD	EFD	Error (%)
0.6	0.0051	0.0053	-3.4	0.0097	0.0102	-5.1	0.0060	0.0064	-5.0
0.8	0.0122	0.0126	-3.0	0.0164	0.0171	-4.0	0.0089	0.0088	1.1
0.9	0.0129	0.0141	-8.1	0.0176	0.0182	-3.1	0.0099	0.0094	5.9
1.0	0.0138	0.0147	-6.4	0.0190	0.0188	0.6	0.0102	0.0096	6.7
1.1	0.0140	0.0148	-5.6	0.0187	0.0188	-0.9	0.0098	0.0094	3.9
1.2	0.0134	0.0143	-6.0	0.0178	0.0182	-2.1	0.0095	0.0090	5.1
1.4	0.0128	0.0128	0.3	0.0164	0.0159	3.4	0.0083	0.0077	8.6
1.6	0.0111	0.0113	-1.9	0.0138	0.0140	-1.7	0.0072	0.0066	9.0
1.8	0.0099	0.0101	-1.8	0.0110	0.0120	-8.5	0.0061	0.0056	7.3
2.0	0.0087	0.0086	1.9	0.0101	0.0102	-0.7	0.0050	0.0047	5.3
2.5	0.0064	0.0063	1.4	0.0078	0.0075	4.7	0.0041	0.0034	21.4

TABLE X. Parameter settings of the irregular wave.

Case ID	Significant wave height, H_s (m)		Peak period, T_p (s)		Computational time (h)
	Full scale	Model scale	Full scale	Model scale	
Case I	5.0	0.102	10.5	1.5	913
Case II	13.0	0.265	14.0	2.0	1763



(a) Case I



(b) Case II

FIG. 14. Time series of wave elevation for irregular waves.

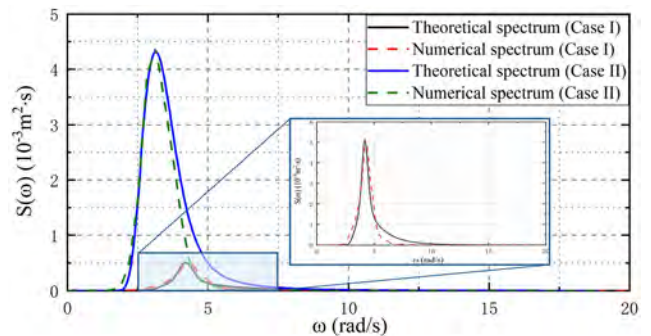


FIG. 15. Comparison of numerical and theoretical spectrum.

ship heave and pitch motion responses between case I and case II can be larger to about 3.5 times and 6 times, respectively.

The exceedance probability, cumulative distribution, and probability density function of hull motion and midship VBM of case I and case II are summarized and fitted with Weibull distribution, as shown

TABLE XI. Wave height statistics of the irregular wave.

Case ID	H_{max}	H_s	H_{mean}	$\frac{H_{max}}{H_s}$	$\frac{H_s}{H_{mean}}$
Case I	0.151	0.096	0.059	1.57	1.63
Case II	0.442	0.265	0.164	1.67	1.62

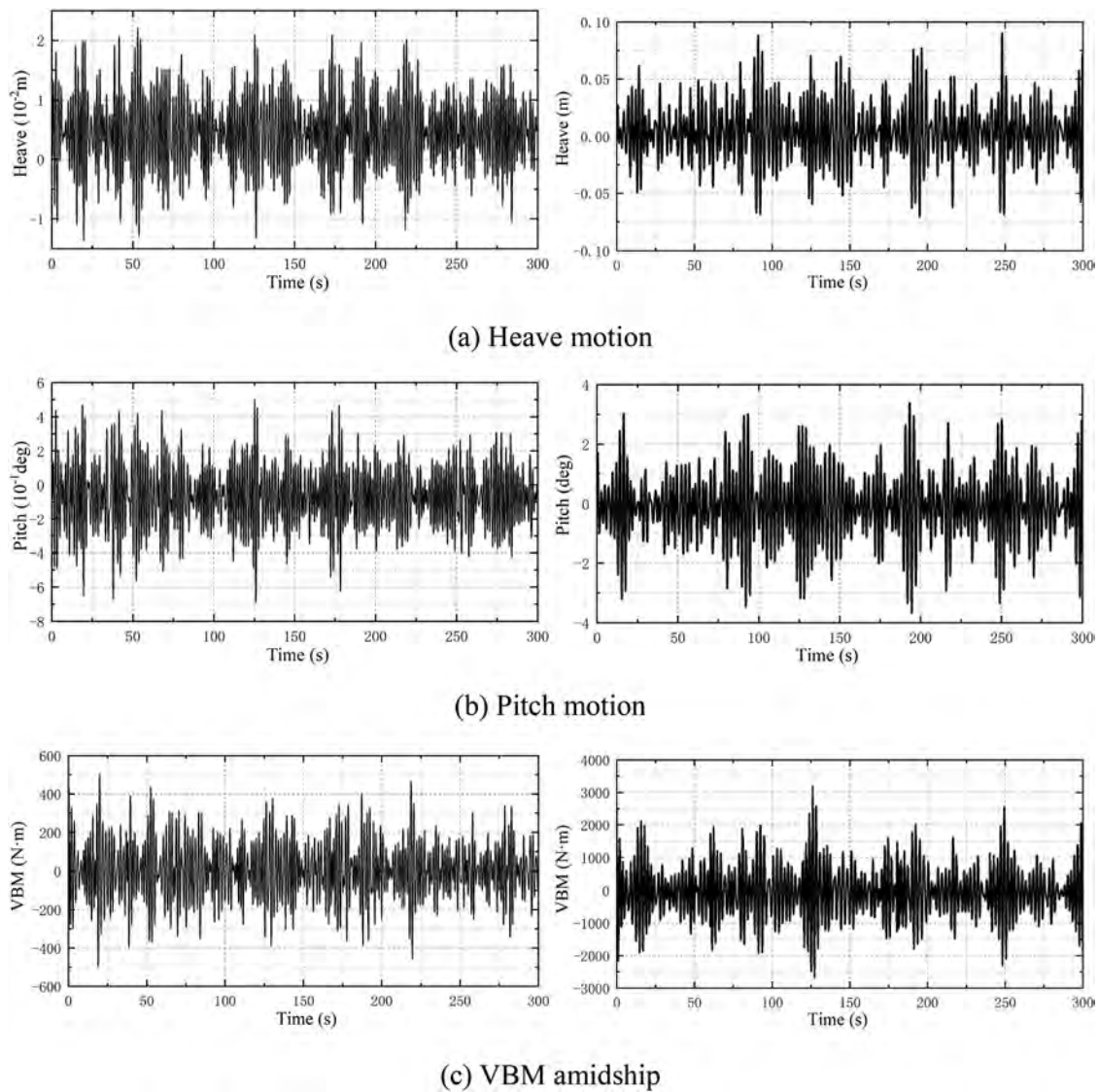


FIG. 16. Time series of ship motions and VBM responses in irregular waves (left, case I; right, case II).

in Figs. 17 and 18, respectively. All the statistical parameters satisfy the Weibull distribution well.

In addition, the maximum, significant, and average values of VBM loads at different stations are counted and summarized. The

longitudinal distribution of VBM loads is illustrated in Fig. 19. It is noticed that for case II, the VBM distribution reaches its maximum peak near the midship position at element 10. For case I, the maximum peak of the VBM load of the significant and average values appears

TABLE XII. Comparison of the amplitude responses of ship motions and VBM amidship in irregular waves with different wave height.

Parameters	Maximum value			Significant value			Average value		
	Case I	Case II	Difference (%)	Case I	Case II	Difference (%)	Case I	Case II	Difference (%)
Heave (mm)	17.5	78.3	347.4	11.2	51.3	358.0	7.2	32.9	356.9
Pitch (deg)	0.59	3.38	472.9	0.32	2.31	621.9	0.21	1.43	580.9
VBM (Nm)	462.6	1465.2	216.7	280.4	802.6	186.2	177.6	529.9	198.4

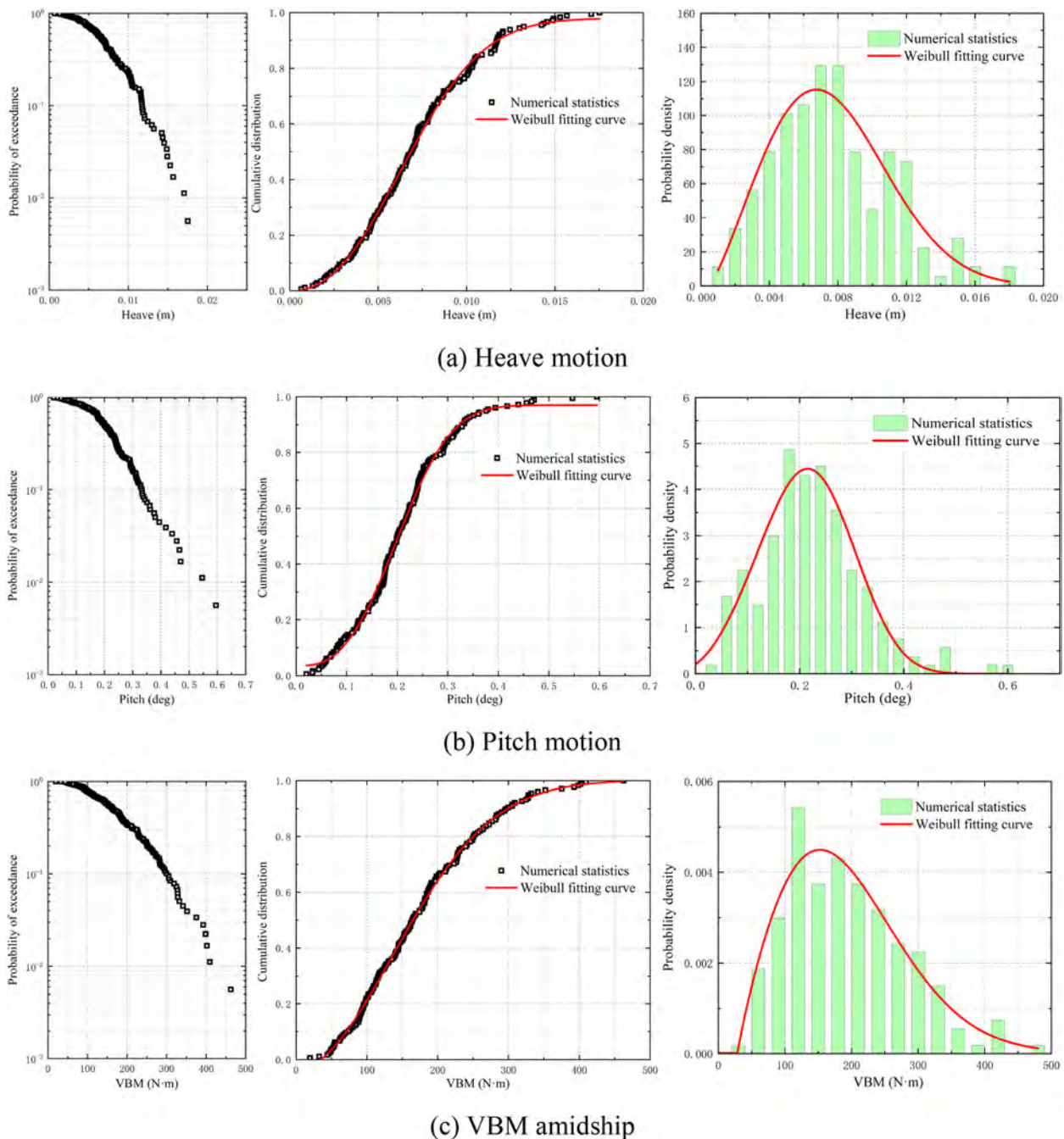


FIG. 17. The statistic results of exceedance probability, cumulative distribution, and probability density function of ship motions and VBM amidship of case I.

near element 12, while the VBM peak of the maximum value appears near the midship at element 11.

Figures 20 and 21 compare the cumulative distribution statistics of pressure sensors at different heights and stations of case I and II, respectively. It is noticed that the distribution of pressure sensors under free surface satisfies both Weibull and normal

distribution. For the sensors above free surface, in case I, the wave impact pressure at the height of Z_8 is zero in most moments, indicating that the wave can hardly reach the height of Z_8 in most time. The wave impact at Z_8 position can only occur when large waves are encountered, and violent ship motions are induced. At the height of Z_{10} , the pressure measurements no longer satisfy the

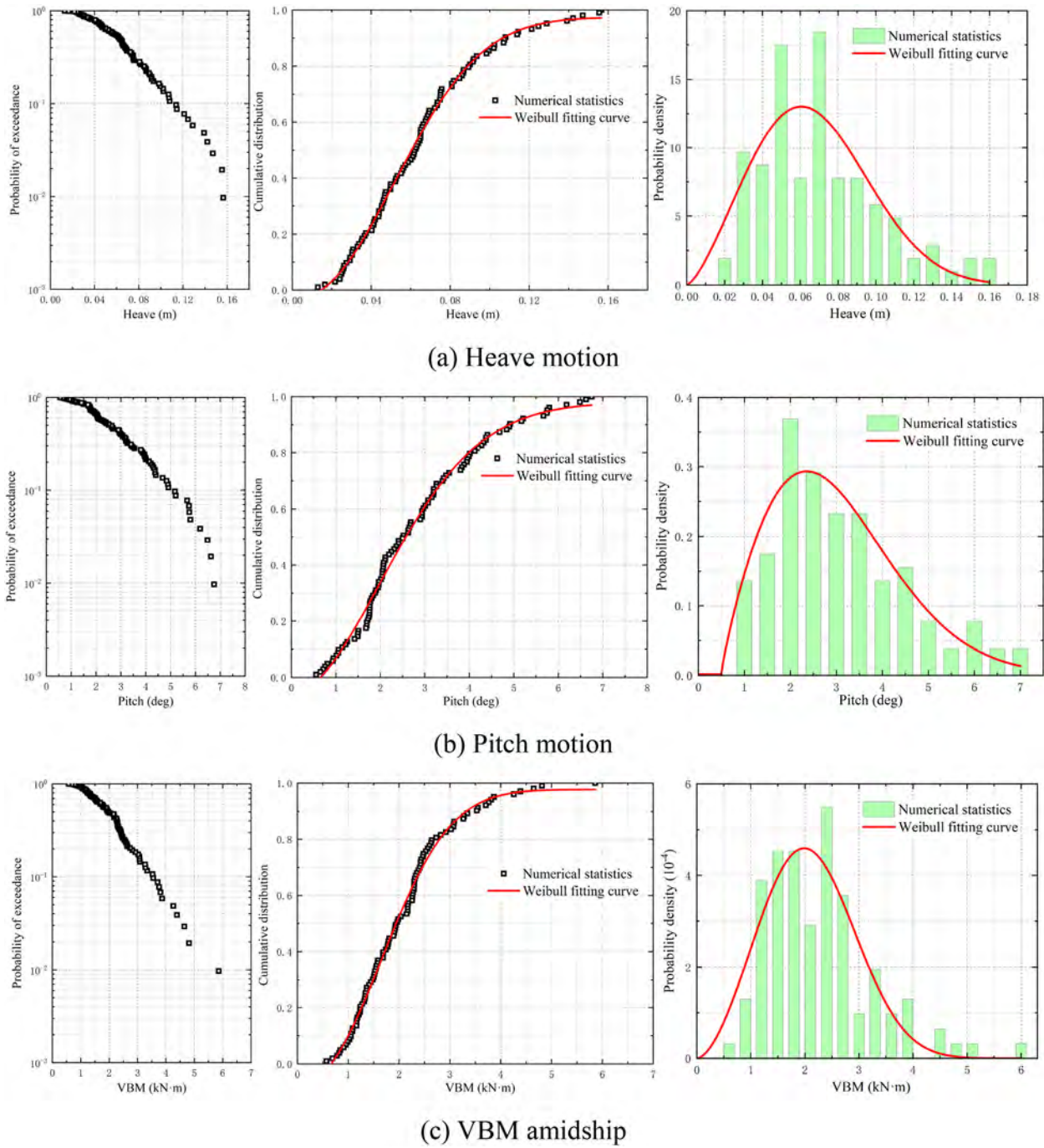


FIG. 18. The statistic results of exceedance probability, cumulative distribution, and probability density function of ship motions and VBM amidship of case II.

Weibull distribution but also satisfy the normal distribution. As a matter of fact, the pressure value at Z_{10} position has always been negative, which is related to the setting of the zero pressure reference point near free surface at the initial time. Therefore, the

pressure value at the position of Z_{10} height mainly reflects the relative change caused by the velocity of air. It is independent with the impact of waves, but the statistic results show that the pressure changes in the air also satisfy a certain statistical distribution. As

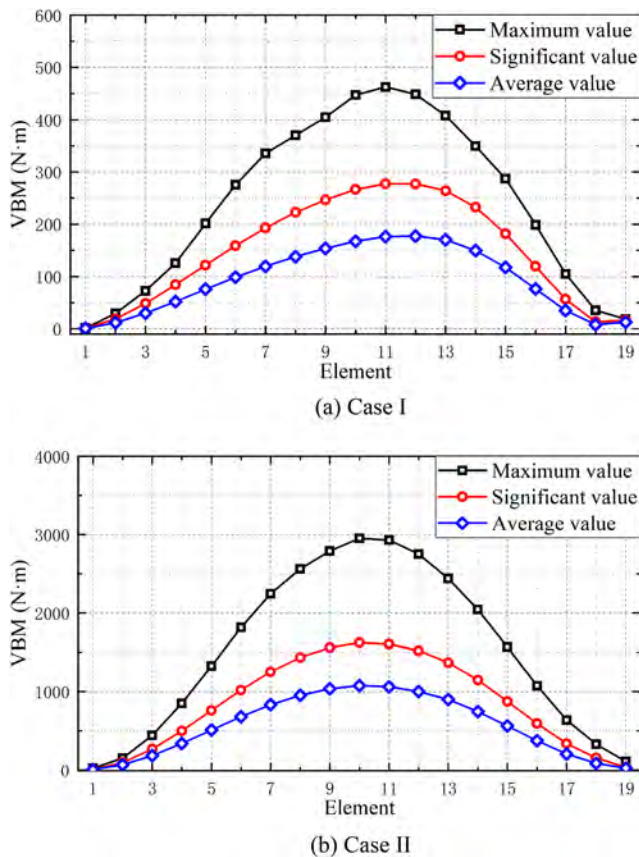


FIG. 19. Longitudinal distribution of VBM loads.

for the sensors above free surface in case II, the wave impact pressure at Z_8 height also satisfies both Weibull and normal distribution. The pressure distribution at Z_{10} height is similar to that at Z_8 height of case I.

The CFD results of wave elevation and impact loads of both cases at four time steps are shown in Figs. 22 and 23. It is seen that at the time step of 19.5 s in case I and the time step of 298.5 s in case II, there is a relative high pressure region on ship bow with the interaction of both ship pitch motion and wave crest. The spatial distribution of wave impact pressure loads mainly satisfy the positive correlation between pressure values and water depth.

The maximum, significant, and average values of wave impact pressure at different positions in case I and case II are summarized in Tables XIII–XV, respectively. It is noticed that on the whole, the closer the pressure sensors are to the baseline, the greater the pressure measurement values become. The closer to the ship bottom, the smaller the relative pressure differences are between different stations. As for case I, the average value of pressure measurements at the height of Z_9 is generally less than zero, indicating that this position is exposed to the air in most time. However, the maximum pressure value is relatively large, meaning that there are individual waves causing the violent motion of the hull and making great wave

impact on the height of Z_9 . As for case II, the difference between maximum value, significant value, and average value of pressure is much bigger than that in case I, implying the more severe slamming happening in case II.

The difference between the maximum values with significant and average values of wave impact pressure of both cases are summarized in Tables XVI and XVII. It is seen that the differences become larger with the sensor position being higher, which indicates that the closer the sensors are to the deck, the greater influence of wave impact pressure by individual large waves. In addition, the differences vary less in case II than in case I. As for higher pressure sensors, the differences are smaller in case II, while as for lower sensors, the differences are bigger in case II. It indicates that for low sea conditions with relative small significant wave height, the large waves have a much greater influence on the slamming pressure response.

The relations of the three values of wave impact pressure are summarized in Fig. 24 and fitted with linear lines. It is noticed that the fitting line of case II has a smaller intercept than that of case I, which indicates that rare wave slamming with larger pressure peaks is detected in the position with higher slamming sensors. The significant value and average value are small because it occurs less. However, once the wave slamming occurs, there will be a higher slamming pressure captured on the pressure sensors.

B. Responses in freak wave

In the numerical simulations of irregular waves for a long time, a wave with a large amplitude of wave height often occurs suddenly, which is known as freak wave. The freak wave in this study is generated with this method. First, a 3-h long-time wave is generated by HOS-NWT solver with the same parameter settings of the irregular wave in Sec. V A and Table X. Then a relative high wave is picked as a freak wave for further study. Figure 25 shows the freak wave appearing from 4775 to 4785 s with significant wave height of 5 m in full scale (case III), and the wave appeared from 2045 to 2055 s with significant wave height of 13 m in full scale (case IV). The freak wave in irregular waves may bring large responses of ship motion and structure loads, and it has always been the research interest in the prediction of wave-structure interactions. The HOS-CFD-MBD method is able to effectively select the segment of time series of wave with high efficiency and then input the selected wave into CFD computational domain for the numerical simulation with high accuracy.

The time series of wave elevation in the CFD computational domain is measured and compared with that of HOS wave, as shown in Fig. 26. It is seen that for the wave components before the single freak wave, the HOS-CFD results show good agreement with the HOS input data, verifying the reliability of the wave generation. For the wave components after the maximum amplitude of the freak wave, the time series of HOS-CFD results and HOS input data show inconsistent characteristics. However, on the whole, the numerical simulation of the freak wave with the coupled HOS-CFD method can effectively capture the main features of the freak wave.

Figure 27 shows the time histories of the ship motions and structural responses in freak waves. Table XVIII summarizes the amplitude responses of heave motion, pitch motion, and VBM amidship between irregular and freak waves with different significant wave heights. It is noticed that for the low wave condition, the responses of freak wave are smaller than that of irregular waves. However, as for high wave

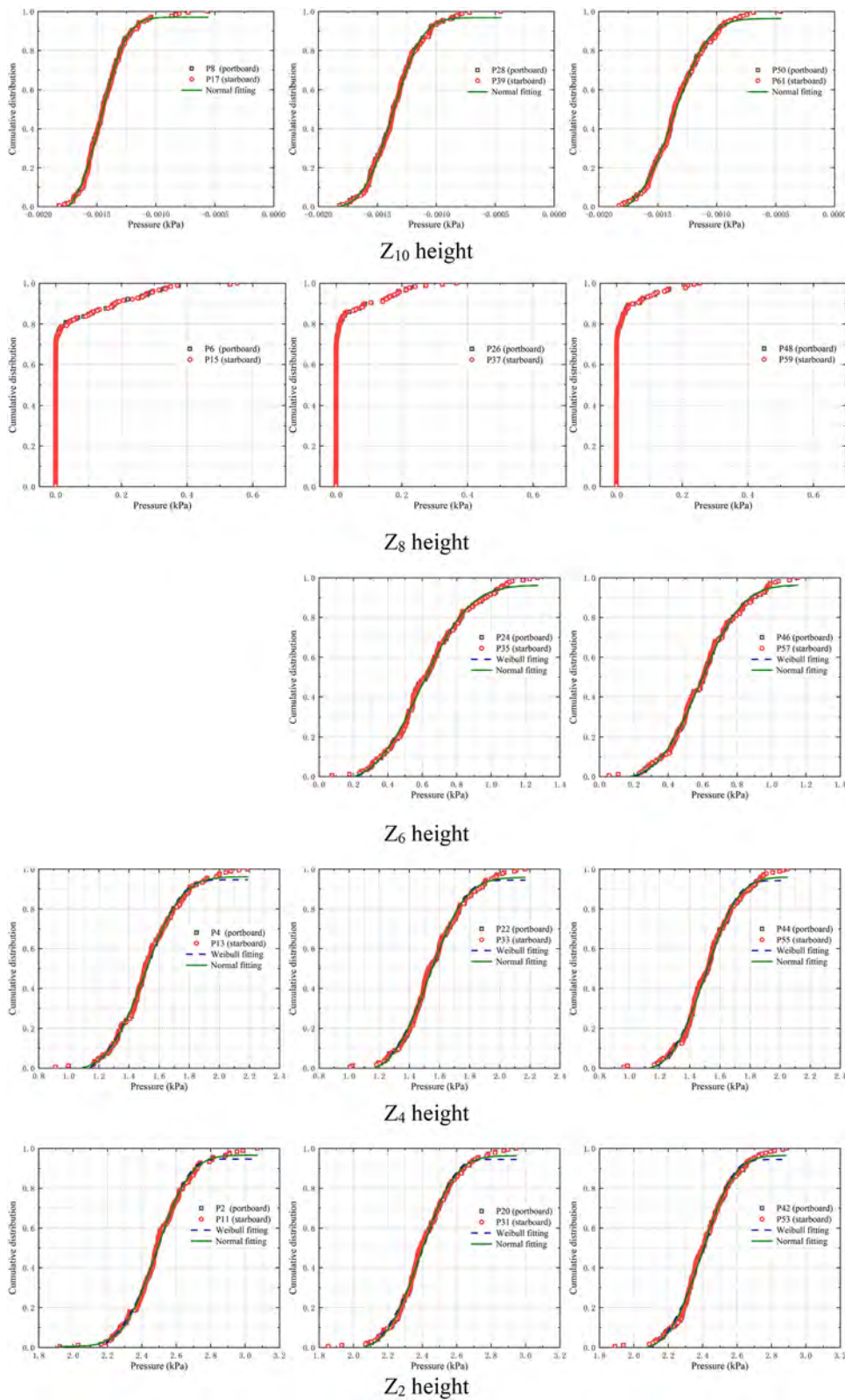


FIG. 20. The cumulative distributions of pressure sensors at St.20 (left), St.19.5 (medium), and St.19 (right) of case I.

25 February 2025 14:44:23

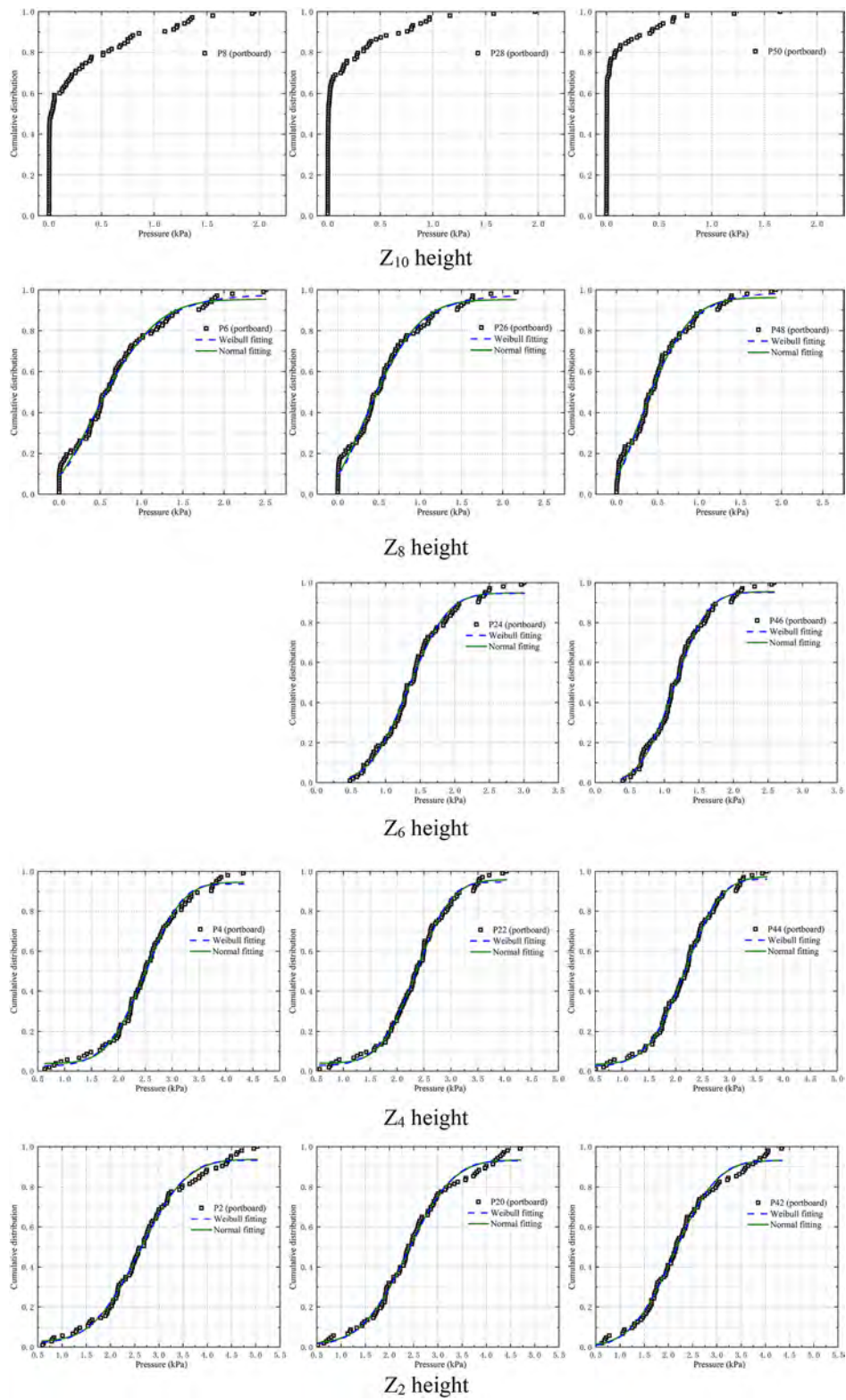


FIG. 21. The cumulative distributions of pressure sensors at St.20 (left), St.19.5 (medium), and St.19 (right) of case II.

25 February 2025 14:44:23

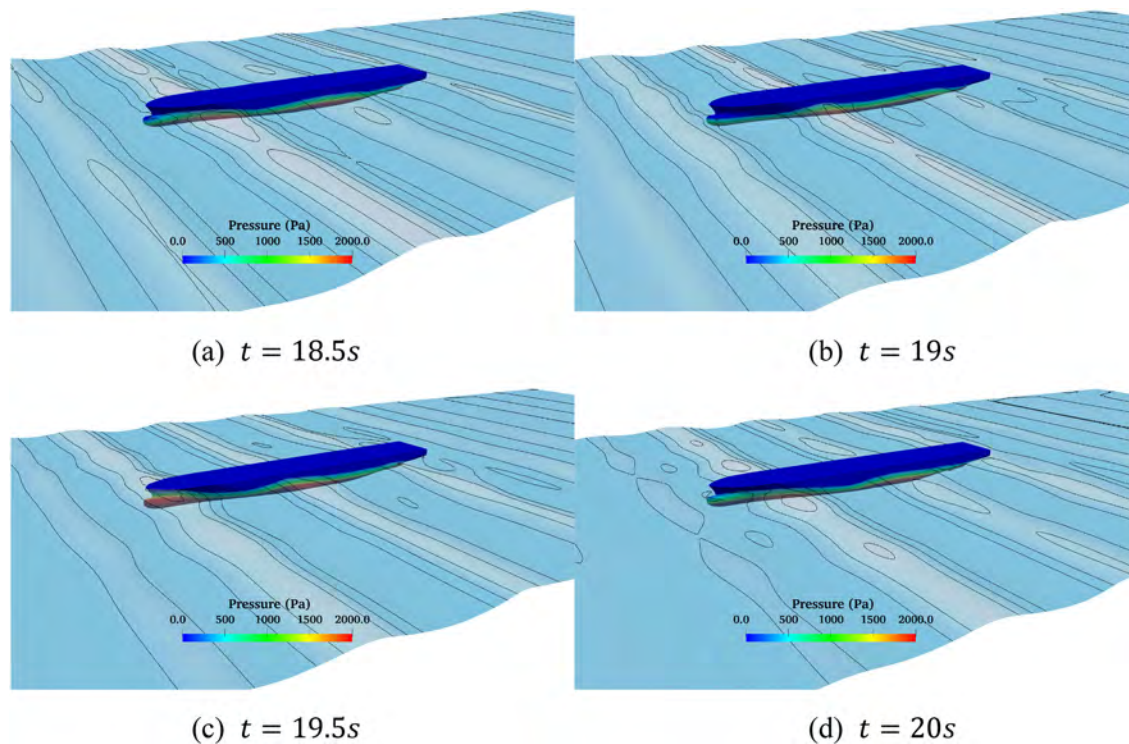


FIG. 22. CFD results of wave elevation and wave impact pressure in case I.

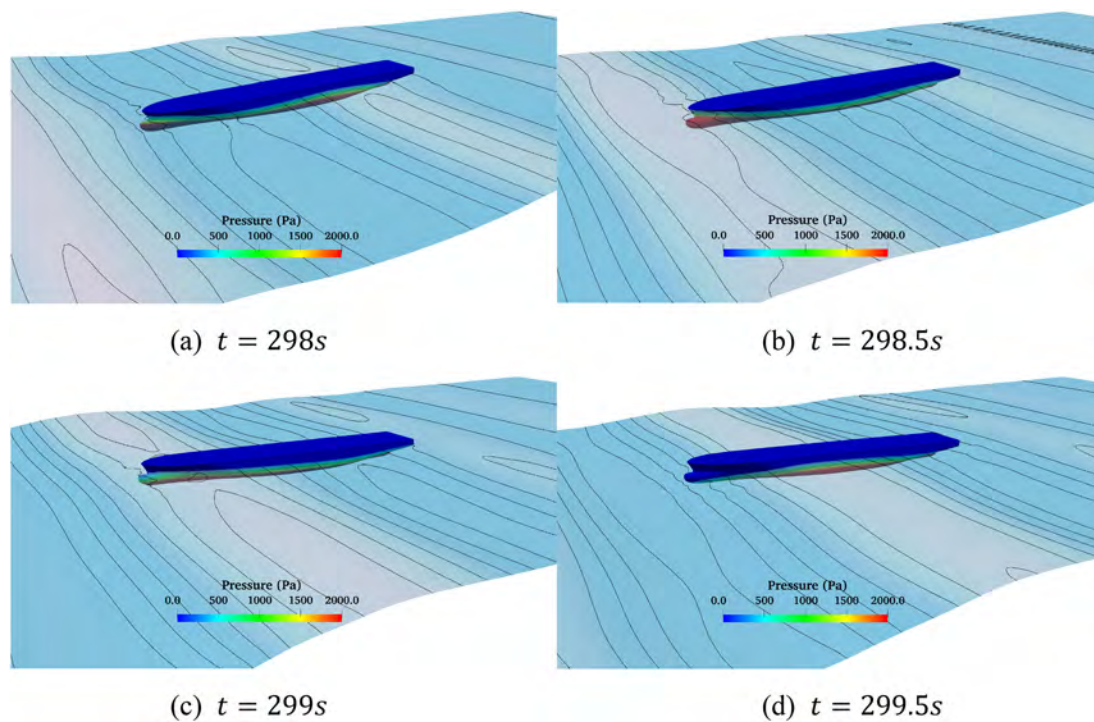


FIG. 23. CFD results of wave elevation and wave impact pressure in case II.

25 February 2025 14:44:23

TABLE XIII. Spatial distribution of maximum values of wave impact pressure peak.

Sensor height	Pressure (Pa) (Case I)			Pressure (Pa) (Case II)		
	St. 20	St. 19.5	St. 19	St. 20	St. 19.5	St. 19
Z ₁₁	-1.35	-1.45	-1.35	2104.10	1824.19	1295.66
Z ₁₀	-0.57	-0.46	-0.47	1948.66	1970.94	1649.27
Z ₉	158.12	50.00	10.38	2354.17	2061.13	1677.77
Z ₈	553.10	367.30	254.42	2507.69	2166.44	1930.29
Z ₇	...	798.36	655.58	...	2601.97	2129.68
Z ₆	...	1272.67	1153.12	...	3004.70	2584.55
Z ₅	1792.98	1742.91	1617.87	3599.96	3333.47	3006.28
Z ₄	2188.83	2170.09	2052.00	4329.62	4032.25	3688.93
Z ₃	2584.68	2543.67	2550.12	4636.51	4330.50	4011.15
Z ₂	3072.29	2947.46	2884.29	5028.68	4708.72	4345.16
Z ₁	3559.90	3435.38	3373.54	5421.02	5020.63	4643.06

TABLE XIV. Spatial distribution of significant values of wave impact pressure.

Sensor height	Pressure (Pa) (Case I)			Pressure (Pa) (Case II)		
	St. 20	St. 19.5	St. 19	St. 20	St. 19.5	St. 19
Z ₁₁	-1.87	-1.92	-1.94	504.04	306.76	138.16
Z ₁₀	-1.21	-1.10	-1.04	795.90	540.31	311.96
Z ₉	5.94	1.86	0.49	1169.39	923.08	578.50
Z ₈	129.40	75.21	51.17	1376.35	1166.74	1007.34
Z ₇	...	430.88	355.29	...	1630.93	1251.17
Z ₆	...	898.21	840.88	...	2039.16	1729.35
Z ₅	1358.34	1366.02	1303.49	2602.55	2409.36	2172.51
Z ₄	1773.91	1801.65	1740.96	3346.54	3097.65	2850.81
Z ₃	2189.49	2190.84	2251.57	3615.52	3378.79	3119.42
Z ₂	2698.81	2610.23	2594.45	3826.65	3598.30	3292.22
Z ₁	3208.13	3116.25	3100.13	3967.92	3607.88	3217.28

TABLE XV. Spatial distribution of average values of wave impact pressure.

Sensor height	Pressure (Pa) (Case I)			Pressure (Pa) (Case II)		
	St. 20	St. 19.5	St. 19	St. 20	St. 19.5	St. 19
Z ₁₁	-2.03	-2.08	-2.09	168.40	103.36	47.68
Z ₁₀	-1.42	-1.34	-1.32	280.40	183.70	105.24
Z ₉	-0.81	-0.60	-0.41	516.88	392.13	208.29
Z ₈	42.63	24.68	16.75	695.20	581.92	509.07
Z ₇	...	197.94	161.45	...	1025.28	739.35
Z ₆	...	640.71	611.93	...	1428.37	1215.17
Z ₅	1096.23	1158.11	1080.50	1894.80	1787.94	1641.80
Z ₄	1533.88	1567.05	1528.12	2530.29	2360.23	2160.31
Z ₃	1971.53	1975.99	2057.96	2667.43	2481.26	2259.61
Z ₂	2502.69	2414.83	2413.91	2719.98	2520.71	2283.12
Z ₁	3033.85	2939.40	2936.91	2739.16	2479.87	2202.41

25 February 2025 14:44:23

TABLE XVI. Comparison of differences between maximum value P_{max} with significant value $P_{1/3}$ and average value \bar{P} of wave impact pressure of case I.

Sensor height	Differences between P_{max} and $P_{1/3}$ (%)			Differences between P_{max} and \bar{P} (%)		
	St. 20	St. 19.5	St. 19	St. 20	St. 19.5	St. 19
Z_9	-96.20	-96.26	-95.27	-100.53	-101.22	-103.93
Z_8	-76.69	-79.47	-79.77	-92.33	-93.26	-93.38
Z_7	...	-45.89	-45.62	...	-75.13	-75.26
Z_6	...	-29.31	-26.97	...	-49.56	-46.82
Z_5	-24.18	-21.41	-19.36	-38.80	-34.46	-33.14
Z_4	-18.91	-16.91	-15.09	-29.88	-27.72	-25.46
Z_3	-15.25	-13.82	-11.66	-23.69	-22.27	-19.25
Z_2	-12.12	-11.40	-10.01	-18.51	-18.03	-16.27
Z_1	-10.02	-9.27	-8.08	-14.22	-14.42	-12.92

TABLE XVII. Comparison of differences between maximum value P_{max} with significant value $P_{1/3}$ and average value \bar{P} of wave impact pressure of case II.

Sensor height	Differences between P_{max} and $P_{1/3}$ (%)			Differences between P_{max} and \bar{P} (%)		
	St. 20	St. 19.5	St. 19	St. 20	St. 19.5	St. 19
Z_9	-50.33	-55.21	-65.52	-78.04	-80.98	-87.59
Z_8	-45.11	-46.15	-47.81	-72.28	-73.14	-73.63
Z_7	...	-37.32	-41.25	...	-60.60	-65.28
Z_6	...	-32.13	-33.09	...	-52.46	-52.98
Z_5	-27.71	-27.72	-27.73	-47.37	-46.36	-45.39
Z_4	-22.71	-23.18	-22.72	-41.56	-41.47	-41.44
Z_3	-22.02	-21.98	-22.23	-42.47	-42.70	-43.67
Z_2	-23.90	-23.58	-24.23	-45.91	-46.47	-47.46
Z_1	-26.81	-28.14	-30.71	-49.47	-50.61	-52.57

condition, the responses in freak wave are higher than that in irregular waves, especially for VBM response. It may indicate that the freak wave with relative large wave height in high wave conditions can be much more dangerous. In addition, in the time series of VBM

responses, it is noticed that there appear significant high order components of VBM responses in high sea condition.

In order to study the possible reasons for the lower responses in freak waves of case III, the structural response of VBM amidship is

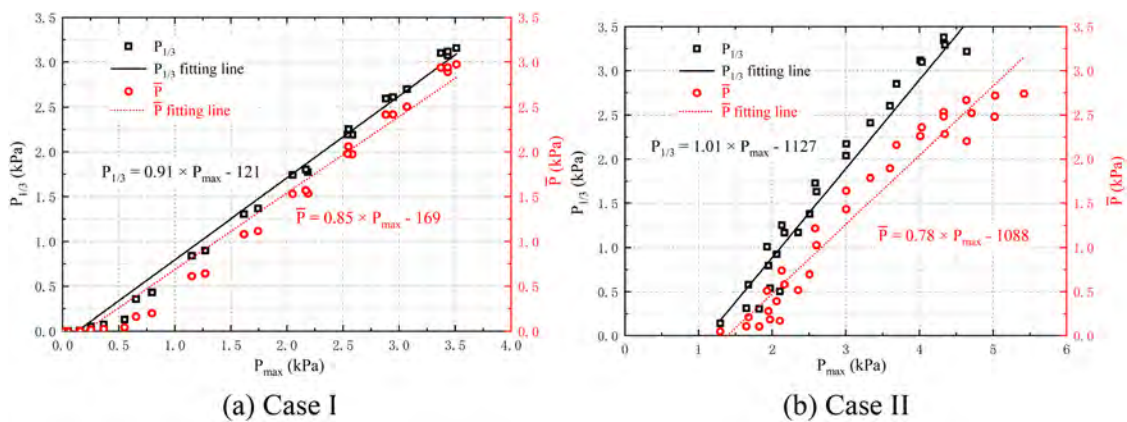


FIG. 24. Relations between maximum, significant, and average values of wave impact pressure.

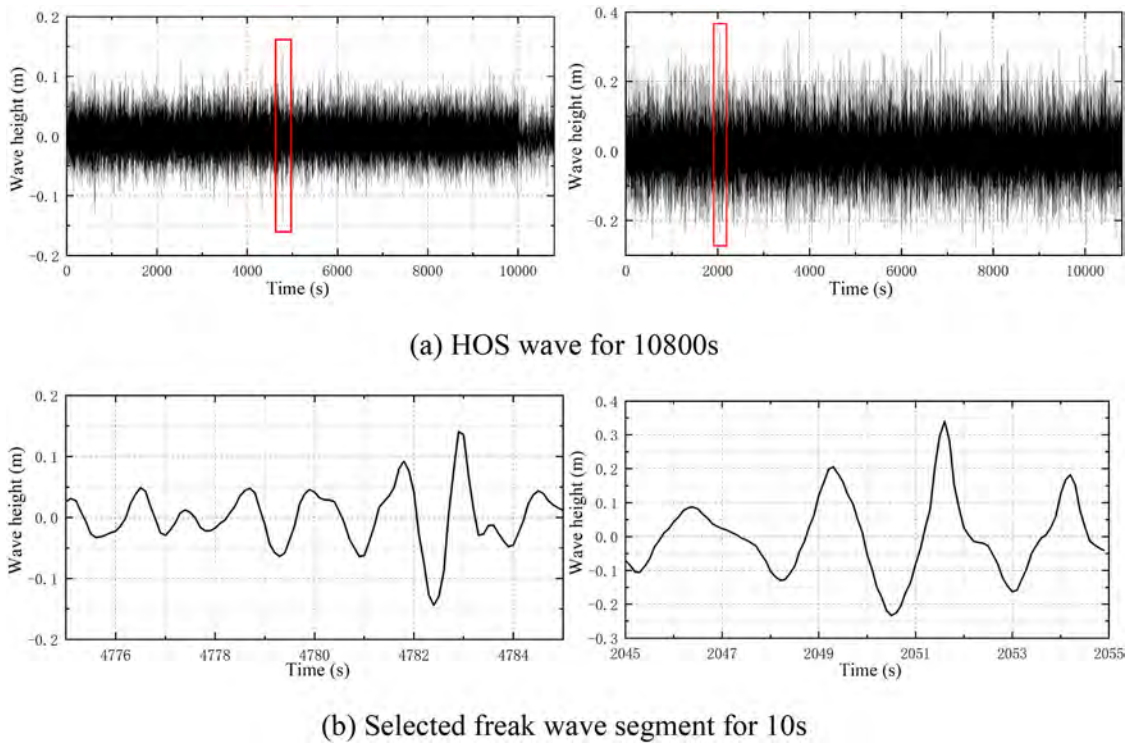


FIG. 25. Time histories of long-time HOS waves and the selected freak wave segment (left, case III; right, case IV).

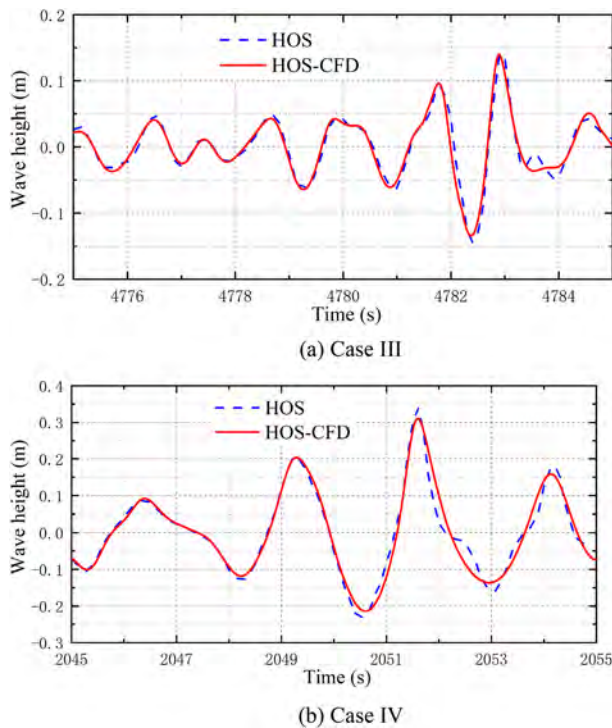


FIG. 26. Comparison of wave elevations between HOS-CFD results and HOS input data.

selected as an example. The time series of wave elevation and VBM are compared together in Fig. 28. Figure 28(a) shows the comparison in irregular waves from 0 to 50 s. It is seen that there is a large peak of VBM happening at around 20 s, while the corresponding large wave height happens at around 17 s, indicating that the responses of VBM amidship happen later than the encountering waves at ship bow. In addition, there are two wave segments with similar wave heights with the time of 15–20 and 36–42 s, while the VBM responses of the latter time segment are significantly smaller than that of former. It implies that in the several consecutive large waves, the gradually larger amplitude of wave height may exacerbate the responses of ship motion and VBM load.

Figures 29 and 30 show the wave elevation and wave impact hydrodynamic loads at different time steps in freak waves. It is noticed that the high pressure area on hull surface of hydrodynamic pressure develops from ship bow to the stern with the wave crest. In case IV of Fig. 30, an obvious phenomenon of green water occurs, and the slamming pressure loads on hull surface are much more severe than that in irregular waves in Fig. 23. The wave load caused by severe slamming and green water can be the main reason for inducing the high frequency response of VBM amidship in Fig. 27(c).

VI. CONCLUSIONS

In this paper, a coupled HOS-CFD-MBD method is adopted in the numerical studies of ship hydroelasticity of a 20 000 TEU container-ship in irregular and freak waves. The two-way coupled FSI

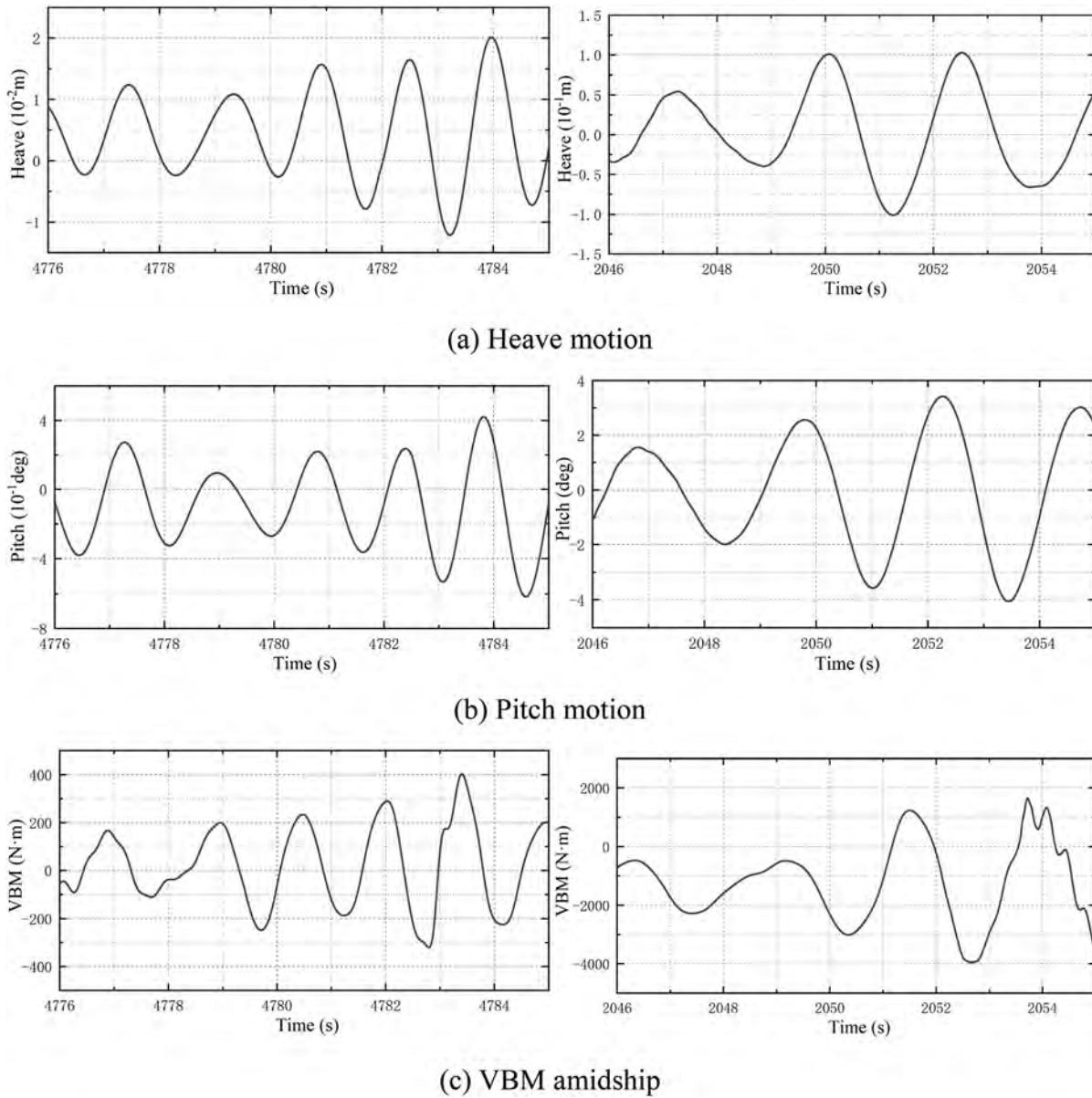


FIG. 27. Time series of the responses of ship motions and VBM amidship in freak waves (left, case III; right, case IV).

TABLE XVIII. Comparison of the amplitude responses of ship motions and VBM amidship between irregular and freak wave results.

Parameters	Hs = 5 m (full scale)			Hs = 13 m (full scale)		
	Irregular wave	Freak wave	Difference (%)	Irregular wave	Freak wave	Difference (%)
Heave (mm)	17.5	16.1	-8.0	78.3	101.8	30.0
Pitch (deg)	0.59	0.52	-11.9	3.38	3.74	10.7
VBM (Nm)	462.6	361.5	-21.9	1465.2	2800.5	91.1

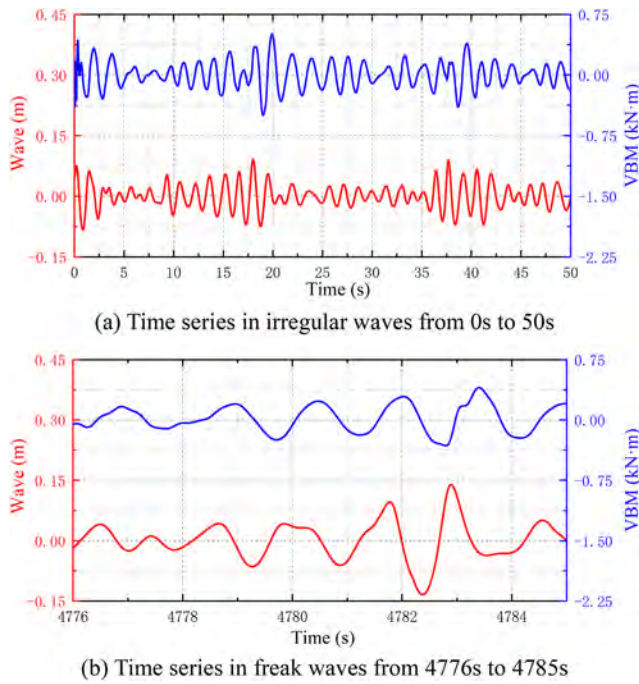


FIG. 28. Comparison of the time histories of wave elevation and VBM amidship in irregular and freak waves of case I and case III.

framework based on CFD-MBD method is applied for the simulation of ship hydroelasticity. The potential-viscous flow coupled HOS-CFD method is adopted in the wave generation for irregular and freak waves. The convergence studies of computational grid and time step are checked. The modal analysis of natural frequency and the hydroelastic responses including ship motions and VBM loads are validated with experimental measurements. In addition, the ship hydroelasticity in irregular and freak waves are studied. The main conclusions obtained are as follows:

- (1) The strong coupled two-way CFD-MBD method is adopted for the numerical predictions of ship motions and structural hydroelastic responses in regular head waves, which agrees well with experimental measurements. With the comparison of VBM responses in different wavelengths, the maximum value of the VBM RAO appears in the condition of $\lambda/L = 1.0$.
- (2) The freak wave generated by HOS-CFD method shows good agreement with the HOS input data, implying the effectiveness of wave making by HOS-CFD method. The cumulative distribution and probability density function of hull motion and VBM amidship are well fitted with Weibull distribution. The cumulative distributions of most sensor pressures are well fitted with both Weibull and normal distributions.
- (3) The amplitude of pitch motion is most sensitive to the wave height of irregular waves. When the significant wave height of the irregular wave increases by 1.6 times, the VBM response increases by about two times, the heave response increases by 3.5 times, and the pitch response increases by about six times.

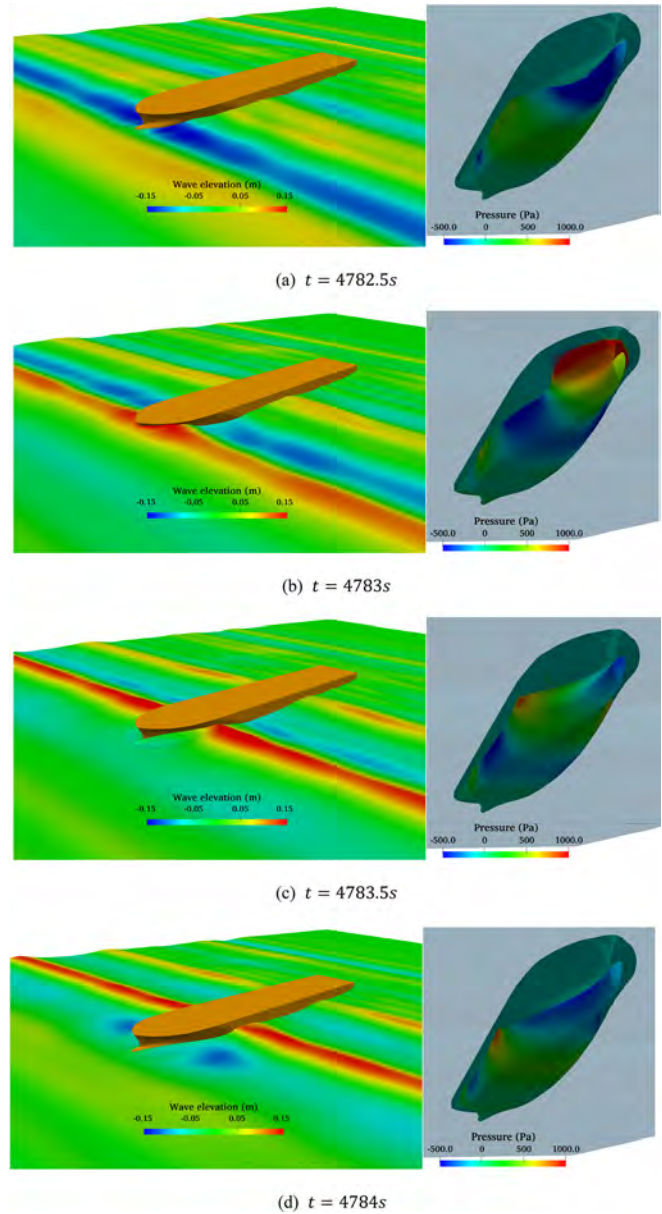


FIG. 29. Wave elevation and wave impact loads in the freak wave of case III.

In high sea states, bow slamming and green water are the main causes of high frequency responses of VBM.

In this study, the ship hydroelastic responses and wave loads in irregular waves are studied without considering the influence of ship speed. In the future, the HOS-CFD-MBD method is planned to be combined with the overset grid technique for the further study of the combination of ship hydroelasticity and maneuverability with ship speed. In addition, the unsymmetrical responses in oblique waves of the ship have also been one of the study interests in the future.

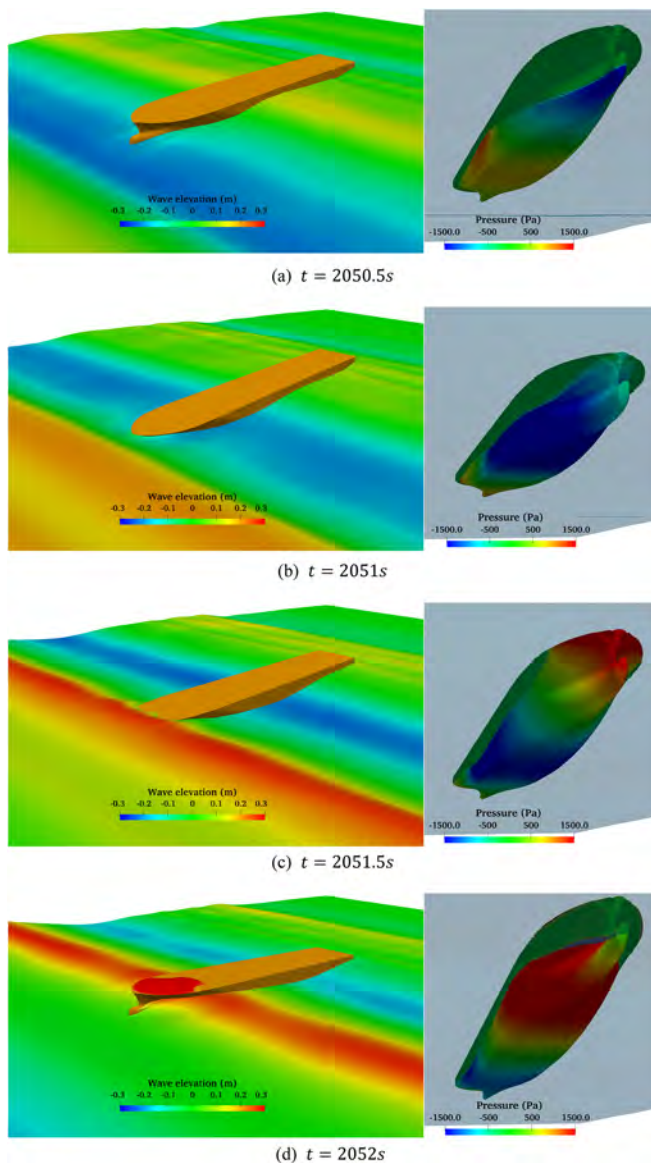


FIG. 30. Wave elevation and wave impact loads in the freak wave of case IV.

ACKNOWLEDGMENTS

This work was supported by the National Natural Science Foundation of China (52471335 and 51809169), to which the authors are most grateful.

AUTHOR DECLARATIONS

Conflict of Interest

The authors have no conflicts to disclose.

Author Contributions

Wenjie Zhang: Data curation (equal); Formal analysis (equal); Investigation (equal); Methodology (equal); Validation (equal);

Visualization (equal); Writing – original draft (equal). **Yuan Zhuang:** Investigation (equal); Methodology (equal); Software (equal). **Decheng Wan:** Resources (equal); Software (equal); Supervision (equal). **Jianhua Wang:** Conceptualization (equal); Funding acquisition (lead); Investigation (equal); Methodology (equal); Software (equal); Supervision (equal); Writing – original draft (equal); Writing – review & editing (lead).

DATA AVAILABILITY

The data that support the findings of this study are available from the corresponding author upon reasonable request.

REFERENCES

- Y. Lu, J. Liu, B. Teng *et al.*, “Modal Investigation on a large-scale containership model for hydroelastic analysis,” *Shock Vib.* **2022**, 1.
- E. V. Lewis, “Ship model test to determine moments in waves,” *Trans. Soc. Nav. Archit. Mar. Eng.* **62**, 426–490 (1954).
- J. C. D. Does and J. C. D. Does, “Experimental determination of bending moments for three models of different fullness in regular waves,” *Int. Shipbuild. Prog.* **7**(68), 139–160 (1960).
- G. J. Grigoropoulos and G. M. Katsaounis, “Measuring procedures for seakeeping tests of large-scaled ship models at sea,” in *13th IMEKO TC4 Symposium on Measurements for Research and Industrial Applications* (IMEKO, Athens, Greece, 2004), pp. 135–139.
- N. Salvesen, *Ship Motions and Sea Loads* (SNAME Transaction, 1970).
- R. E. D. Bishop and W. G. Price, *Hydroelasticity of Ships* (Cambridge University Press, 1979).
- Y. S. Wu, H. Maeda, and T. Kinoshita, “The second order hydrodynamic actions on a flexible body,” *J. Inst. Ind. Sci., Univ. Tokyo* **49**(4), 8–19 (1997).
- H. Y. Tang, H. L. Ren, H. Li *et al.*, “Experimental investigation of wave-induced hydroelastic vibrations of Trimaran in oblique irregular waves,” *Shock Vib.* **2016**, 8794560.
- H. Hashimoto, S. Yoneda, T. Omura *et al.*, “CFD prediction of wave-induced forces on ships running in irregular stern quartering seas,” *Ocean Eng.* **188**, 106277 (2019).
- J. L. Jiao, H. L. Ren, and C. G. Soares, “Vertical and horizontal bending moments on the hydroelastic response of a large-scale segmented model in a seaway,” *Mar. Struct.* **79**, 103060 (2021).
- D. Kim and T. Tezdogan, “CFD-based hydrodynamic analyses of ship course keeping control and turning performance in irregular waves,” *Ocean Eng.* **248**, 110808 (2022).
- B. Y. Xie, G. H. He, C. K. Zhao *et al.*, “Experimental and numerical investigation on the hydroelastic response of barge and KVLCC2 ship,” *Ocean Eng.* **307**, 118081 (2024).
- X. J. Chen, T. Moan, and S. X. Fu, “Extreme response of very large floating structure considering second-order hydroelastic effects in multidirectional irregular waves,” *J. Offshore Mech. Arct. Eng.* **132**, 041601 (2010).
- Y. Cheng, C. Y. Ji, G. J. Zhai *et al.*, “Hydroelastic analysis of oblique irregular waves with a pontoon-type VLFS edged with dual inclined perforated plates,” *Mar. Struct.* **49**, 31–57 (2016).
- Z. Y. Chen, H. B. Gui, P. S. Dong *et al.*, “Numerical and experimental analysis of hydroelastic responses of a high-speed trimaran in oblique irregular waves,” *Int. J. Nav. Archit. Ocean Eng.* **11**, 409–421 (2019).
- J. L. Jiao, H. C. Yu, C. H. Chen *et al.*, “Time-domain numerical and segmented model experimental study on ship hydroelastic responses and whipping loads in harsh irregular seaways,” *Ocean Eng.* **185**, 59–81 (2019).
- J. L. Jiao, Y. Jiang, H. Zhang *et al.*, “Predictions of ship extreme hydroelastic load responses in harsh irregular waves and hull girder ultimate strength assessment,” *Appl. Sci.* **9**, 240 (2019).
- C. Jin, F. P. Bakti, and M. H. Kim, “Multi-floater-mooring coupled time-domain hydro-elastic analysis in regular and irregular waves,” *Appl. Ocean Res.* **101**, 102276 (2020).

- ¹⁹S. Michele, S. M. Zheng, F. Buriani *et al.*, “Floating hydroelastic circular plate in regular and irregular waves,” *Eur. J. Mech. B* **99**, 148–162 (2023).
- ²⁰P. A. K. Lakshminarayana and S. Hirdaris, “Comparison of nonlinear one- and two-way FFSI methods for the prediction of the symmetric response of a containership in waves,” *Ocean Eng.* **203**, 107179 (2020).
- ²¹J. L. Jiao, S. X. Huang, S. Wang *et al.*, “A CFD–FEA two-way coupling method for predicting ship wave loads and hydroelastic responses,” *Appl. Ocean Res.* **117**, 102919 (2021).
- ²²G. J. Liu, “Research on the nonlinear ship hydroelasticity based on CFD–FEM two-way coupling method,” Ph.D. thesis (Dalian University of Technology, Dalian, 2021).
- ²³Y. C. Liu, Q. Xiao, A. Incecik *et al.*, “Aeroelastic analysis of a floating offshore wind turbine in platform-induced surge motion using a fully coupled CFD–MBD method,” *Wind Energy* **22**(1), 1–20 (2019).
- ²⁴Y. J. Wei, A. Incecik, and T. Tezdogan, “A hydroelasticity analysis of a damaged ship based on a two-way coupled CFD–DMB method,” *Ocean Eng.* **274**, 114075 (2023).
- ²⁵Y. J. Wei, S. R. Yu, P. Jin *et al.*, “Coupled analysis between catenary mooring and VLFS with structural hydroelasticity in waves,” *Mar. Struct.* **93**, 103516 (2024).
- ²⁶W. J. Zhang, J. H. Wang, H. Guo *et al.*, “Numerical investigations of ship hydroelasticity of a 20,000 TEU containership based on CFD–MBD method,” *Ocean Eng.* **317**, 120061 (2025).
- ²⁷Y. Li and M. Lin, “Regular and irregular wave impacts on floating body,” *Ocean Eng.* **42**, 93–101 (2012).
- ²⁸J. L. Jiao, S. X. Huang, and C. G. Soares, “Numerical investigation of ship motions in cross waves using CFD,” *Ocean Eng.* **223**, 108711 (2021).
- ²⁹S. X. Huang, Z. Q. Hu, and C. H. Chen, “Application of CFD–FEA coupling to predict hydroelastic responses of a single module VLFS in extreme wave conditions,” *Ocean Eng.* **280**, 114754 (2023).
- ³⁰G. Ducrozet, F. Bonnefoy, D. L. Touze *et al.*, “A modified high-order spectral method for wavemaker modeling in a numerical wave tank,” *Eur. J. Mech. B* **34**, 19–34 (2012).
- ³¹D. G. Dommermuth and D. K. P. Yue, “A high-order spectral method for the study of nonlinear gravity waves,” *J. Fluid Mech.* **184**, 267–288 (1987).
- ³²B. J. West, K. A. Brueckner, R. S. Janda *et al.*, “A new numerical method for surface hydrodynamics,” *J. Geophys. Res. Oceans* **92**(11), 11803–11824, <https://doi.org/10.1029/JC092iC11p11803> (1987).
- ³³I. Gatin, V. Vukcevic, and H. Jaska, “A framework for efficient irregular wave simulations using higher order spectral method coupled with viscous two phase model,” *J. Ocean Eng. Sci.* **2**(4), 253–267 (2017).
- ³⁴J. Q. Song and D. C. Wan, “Application of coupling model based on High-Order Spectral method and CFD calculation in simulating irregular waves,” *Chin. J. Hydrodyn.* **34**(1), 1–12 (2019).
- ³⁵Y. Zhuang and D. C. Wan, “Parametric study of a new HOS–CFD coupling method,” *J. Hydrodyn.* **33**(1), 43–54 (2021).
- ³⁶H. Rusche, “Computational fluid dynamics of dispersed two-phase flows at high phase fractions,” Ph.D. thesis (University of London, 2002).
- ³⁷F. R. Menter, “Two-equation eddy-viscosity turbulence models for engineering applications,” *AIAA J.* **32**(8), 1598–1605 (1994).
- ³⁸Y. M. Choi, M. Gouin, G. Ducrozet *et al.*, “Grid2Grid: HOS wrapper program for CFD solvers,” arXiv: 1801.00026 (2017).
- ³⁹N. G. Jacobsen, D. R. Fuhrman, and J. Fredsoe, “A wave generation toolbox for the open-source CFD library: OpenFoam,” *Int. J. Numer. Methods Fluids* **70**(9), 1073–1088 (2012).
- ⁴⁰IACS, *Standard Wave Data, IACS Recommendation* (IACS, 2022), p. 34.
- ⁴¹P. Masarati and M. Morandini *et al.*, “An efficient formulation for general-purpose multibody/multiphysics analysis,” *J. Comput. Nonlinear Dyn.* **9**(4), 041001 (2014).
- ⁴²B. Simeon, “On Lagrange multipliers in flexible multibody dynamics,” *Comput. Methods Appl. Mech. Eng.* **195**, 6993–7005 (2006).
- ⁴³E. J. Haug, “An ordinary differential equation formulation for multibody dynamics: Nonholonomic constraints,” *J. Comput. Inf. Sci. Eng.* **17**(1), 011009 (2017).
- ⁴⁴G. L. Ghiringhelli, P. Masarati, and P. Mantegazza, “Multibody implementation of finite volume C^0 beams,” *AIAA J.* **38**(1), 131–138 (2000).
- ⁴⁵W. X. Xiao, C. Liu, B. B. Han *et al.*, “A two-way coupled fluid–structure interaction method for predicting the slamming loads and structural responses on a stiffened wedge,” *Phys. Fluids* **36**, 077123 (2024).
- ⁴⁶J. L. Jiao, S. X. Huang, T. Tezdogan *et al.*, “Slamming and green water loads on a ship sailing in regular waves predicted by a coupled CFD–FEA approach,” *Ocean Eng.* **241**, 110107 (2021).
- ⁴⁷J. H. Wang and W. W. Zhao *et al.*, “Development of naoe-FOAM–SJTU solver based on OpenFOAM for marine hydrodynamics,” *J. Hydrodyn.* **31**(1), 1–20 (2019).
- ⁴⁸H. L. Si, P. Yang, X. K. Gu *et al.*, “Uncertainty analysis of linear vertical bending moment in model tests and numerical prediction,” *Mech. Syst. Sig. Process.* **178**, 109331 (2022).
- ⁴⁹B. V. Divinsky, V. V. Fomin, R. D. Kosyan *et al.*, “Extreme wind waves in the Black Sea,” *Oceanologia* **62**, 23–30 (2020).